The effect of wakes on leading edge loss

Swiss Federal Institute of Technology, ETH Zürich
Institute of Energy Technology, IET
Turbomachinery Laboratory, LSM

Alessandro Sofia

THE EFFECT OF WAKES ON LEADING EDGE LOSS

A Thesis for the degree of Master of Science ETH in Mechanical Engineering.

Project undertaken at the Whittle Laboratory, University of Cambridge, Great Britain.

Supervisors:
Dr. Martin G. Rose, ETH Zürich
Dr. Robert J. Miller, University of Cambridge

Winter semester 2005/2006

ETH
Eidgenössische Technische Hochschule Zürich
Swiss Federal Institute of Technology Zurich

UNIVERSITY OF CAMBRIDGE

PREFACE

After five years at the ETH in Zürich, I decided it was time to move for a while and live a new experience. In Cambridge I had the possibility to run a piece of research in an advanced laboratory and to enjoy the social involvement that living in a college may offer. It was exactly the kind of experience I was looking for.

All my gratitude goes to those who made this experience possible: Dr. Martin Rose, for having recommended me to the Whittle Laboratory and for his supervision; Dr. Rob Miller, who allowed me to join him at the Whittle and was my supervisor; Prof. Dr. Reza Abhari for his permission and finally Dr. Revd. Keith Straughan, who gave me the possibility to become a member of Sidney Sussex College.

Many thanks also to the staff and students of the Whittle, especially to my desk-neighbours of the Hawthorne room and in particular to Davide Giacchè, for his help on the routine for the geometry modification, and Andrew Wheeler, who patiently followed my project, step by step. Without his help, the reported work would have taken twice as much time. Thanks also to Michael Whibley, for his superb work on the prototype blades.

Lugano, 11.5.2006

Alessandro Sofia

ABSTRACT

Efficiency is the key design parameter in today's aeronautical engine industry. In axial compressor blades, the leading edge is the crucial part: its geometry and the way it interacts with the incoming wakes has decisive effects on the boundary layer characters and therefore on the loss.

This work aims to investigate the effect of the leading edge geometry on the performances of a compressor stage. In particular, the interaction between the leading edge and the wake coming from the upstream blade row should be investigated. Gaining some understanding of the physics of this complex process and, more in general, of the behaviour of the flow around the leading edge could lead to the design of optimised geometries with improved performances.

In this work, three geometries have been tested: a high wedge angle blade (32°) with circular leading edge and two newly designed low wedge angle blades (15°) with circular and elliptic (3:1 axes ratio) leading edges, representative of real engine blades. Both numerical and experimental investigations in a low speed axial compressor have been undertaken, in both time averaged and time resolved manner.

The reported results show that designing the leading edge geometry in order to avoid the leading edge separation bubble to appear, may lead to significant loss reduction. A high wedge angle and an elliptic shaped leading edge proved to be able to achieve this. A comparison with the test case with circular leading edge and low wedge angle showed a 25% drop in the loss coefficient.

This encouraging result gives an idea of the big potential of improvement offered by the research on compressor leading edges.

TABLE OF CONTENTS

NOMENCLATURE

a	[mm]	Short semi-axis
A	[-]	Calibration constant
b	[mm]	Long semi-axis
c_f	[-]	Friction coefficient
c_p	[-]	Pressure coefficient
C_{dyn}	[-]	Dynamic head calibration coefficient
C_{stag}	[-]	Stagnation calibration coefficient
C_{yaw}	[-]	Yaw calibration coefficient
E	[V]	Voltage
H	[-]	Shape factor
K	[1/m]	Curvature
K	[-]	Constant
ℓ	[m]	Length
m'	[-]	Arc length coordinate (Mises)
n	[-]	Calibration constant
n	[m]	Normal coordinate
OHR	[-]	Overheat ratio
p	[Pa]	Pressure
p_{A1}	[Pa]	Pressure of tapping A1
p_{D2}	[Pa]	Pressure of tapping D2
p_{in}	[Pa]	Inlet pressure
p_{out}	[Pa]	Outlet pressure
p_{tot}	[Pa]	Total pressure
p^{mixed}	[Pa]	Mixed averaged pressure
p^{ref}	[Pa]	Reference pressure
r	[m]	Radial coordinate
R	[-]	Residuum
R	[Ω]	Resistance
Re	[-]	Reynolds number
S_1	[-]	Inlet slope (Mises)
T	[°C]	Temperature
U	[m/s]	Blade velocity
u	[m/s]	Fluid velocity

v_x	[m/s]	Axial velocity
v_θ	[m/s]	Tangential velocity
x	[m]	x-coordinate, axis
y	[m]	y-coordinate, axis
Y_p	[-]	Loss coefficient
z	[m]	z-coordinate, axis (Mises)
α	[°]	Flow angle (absolute)
α_w	[°]	Flow angle with wake (absolute)
β	[°]	Flow angle (relative)
β_w	[°]	Flow angle with wake (relative)
ϕ	[-]	Flow coefficient
θ	[°]	Tangential angle
θ	[mm]	Momentum thickness
θ_{TE}	[mm]	Trailing edge momentum thickness
θ_0	[mm]	Leading edge momentum thickness
ρ	[kg/m^3]	Density
ρ	[Ω.m]	Resistivity

LIST OF FIGURES

1 INTRODUCTION

1.1 MOTIVATIONS

This work is part of an ongoing project at the Whittle Laboratory, aiming to study compressor leading edges and their interaction with the incoming wakes. This research topic aims to gain some understanding about the physics of the interaction between wakes and boundary layers and about the influence that a specifically tuned leading edge geometry can have on the character of the boundary layer and on the performance of a compressor airfoil.

A large potential of improvement is believed to lay behind this topic. Optimized leading edge geometries may lead to significant improvements in the performance, raising the efficiency of compressor stages of aeronautical engines.

1.2 PROJECT GOALS

First goal of the work is to modify the shape of an existing blade and obtain two new profiles with new leading edge geometry. These must be representative of real engine blades. A blade with circular leading edge and one with elliptic leading edge have to be designed.

Using the computational fluid dynamics (CFD) package Mises (see appendix), a two dimensional, steady analysis must be performed on the airfoil at mid-height of the designed three dimensional blades.

The test blades have then to be built and tested experimentally in the Deverson compressor rig of the Whittle Laboratory (see 5.1). The experiment should point to the measurement of loss: time averaged Y_p measurements and time resolved trailing edge momentum thickness measurements are wanted.

Final goal is to investigate the boundary layer (in unsteady manner) to gain some understanding on the interaction between wakes and leading edge. The unsteady mechanisms of loss production related with the wake interaction and the effect of the different geometries on it are the focus of this analysis.

2 LITERATURE REVIEW

2.1 FLOW AROUND THE LEADING EDGE OF A COMPRESSOR BLADE

2.1.1 SUCTION SPIKE AND SEPARATION BUBBLE

The flow around the leading edge of a compressor blade is described in [3] and [7]. The flow impinges on the leading edge at the stagnation point and then splits and flows onto the pressure or suction surface.

Because of the curvature of the leading edge, the flow strongly accelerates as it goes around it; then it decelerates when it meets the relatively flat surface. The suction and pressure surfaces are not flat, but their curvature is much smaller than that of the leading edge. The leading edge can therefore be seen as a circle and two straight lines tangent to it. The two tangent points are the wedge points.

The rapid acceleration and deceleration around the leading edge causes a peak in the c_p distribution. The steep deceleration on the downward side of the spike can cause the flow to separate, to undergo transition and to reattach as a turbulent boundary layer, forming a separation bubble.

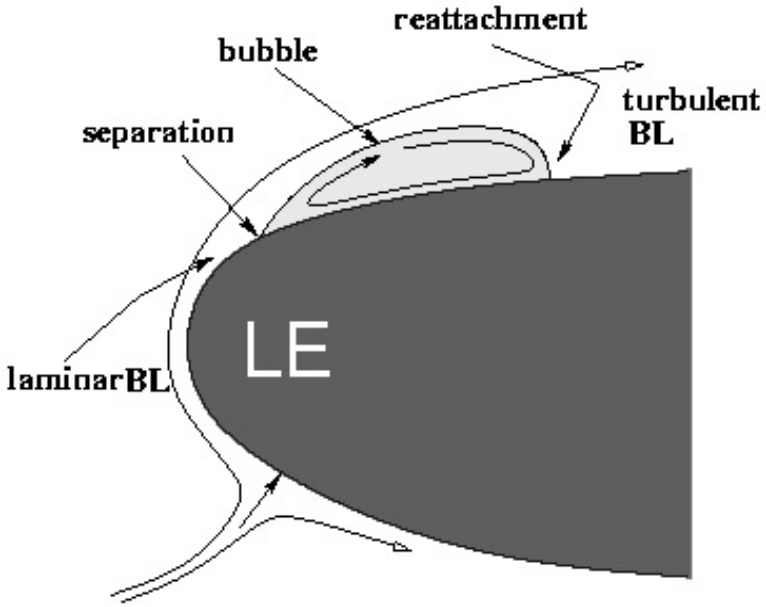

Figure 2.1-1: Leading edge separation bubble

The characteristics of the separation bubble and the mechanisms of transition and reattachment are shortly reviewed here as explained in [1] and [8]. The separated laminar boundary layer gives a laminar shear flow, which is very unstable and goes into transition. A turbulent shear layer originates; this entrains fluid from the external stream and grows rapidly. As a result, the turbulent layer bends toward the wall and reattaches forming the bubble. Since the separated region cannot support any pressure gradient, a small plateau of static pressure (or at least a kink) can be observed in the distribution of the non dimensional pressure coefficient c_p, defined as follows.

$$c_p = \frac{p_{tot,in} - p}{p_{tot,in} - p_{in}} \qquad \textit{Eq. 2.1-1}$$

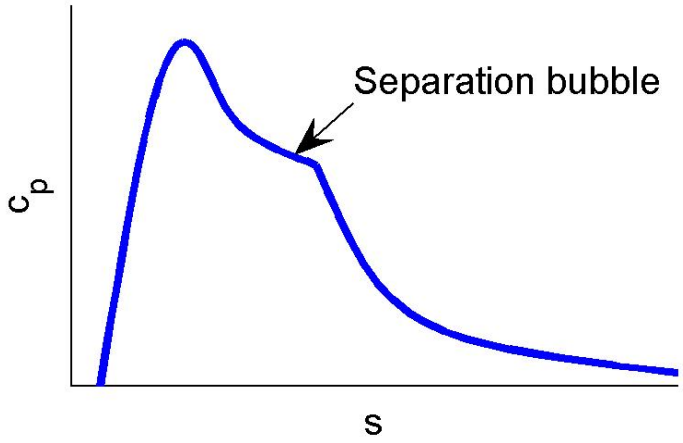

Figure 2.1-2: Leading edge spike and separation bubble

2.1.2 CIRCLE VERSUS ELLIPSE

The shape of the leading edge is a key parameter to influence the size and the characteristics of the separation bubble. This topic has been intensively investigated, for example in [8], where a flat plate with different leading edge geometries has been studied. Similarly to this work, circular and elliptic leading edges have been tested, and the elliptic one has proved better performances in reducing the size of the bubble and making the reattachment possible at higher incidence.

An attempt to analytically explain the benefits of an elliptic leading edge in comparison to a circular one is presented here. As described in the previous paragraph, the curvature of the leading edge forces the flow to accelerate. This

can be understood considering the following momentum conservation equation.

$$\frac{\partial p}{\partial n} = K \cdot \rho \cdot u^2 \qquad \textit{Eq. 2.1-2}$$

With K being the local streamline curvature and having the dimension $1/\ell$.

Regions of high convex curvature of the streamlines are associated with low pressure and high velocity. Furthermore, the radial pressure gradient is proportional to the curvature.

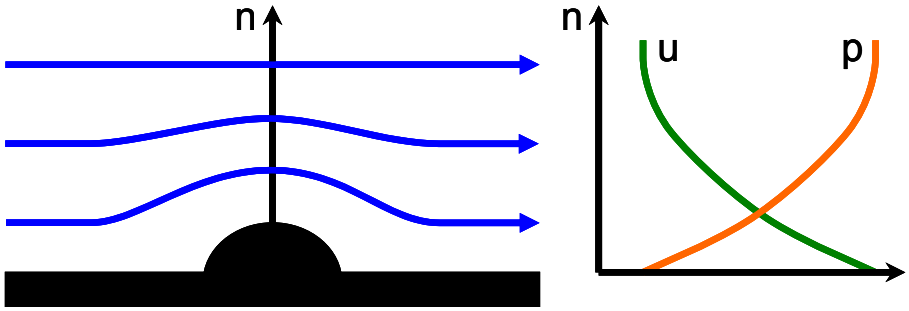

Figure 2.1-3: Streamline curvature

Equation Eq. 2.1-2 shows also that the sudden drop in curvature occurring at the wedge point causes a drop in the radial pressure gradient and a steep deceleration. This strong diffusion can eventually cause the separation. It is now clear that a large discontinuity in curvature should be avoided in order to prevent the separation bubble to appear at the wedge point.

A circle is a geometric figure characterised by a constant curvature being equal to $1/r$. A circular leading edge is therefore a region of constant curvature followed by a flat region. At the wedge point, the curvature suddenly drops to zero.

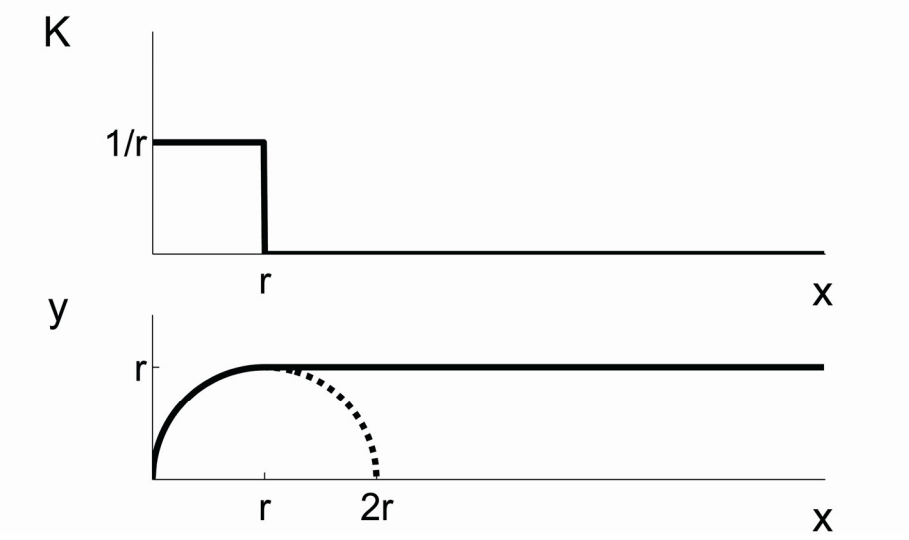

Figure 2.1-4: Curvature of a flat plate with circular leading edge

An ellipse with semi-axes a and b (with a>b), on the other hand, has a high curvature at its sharp side, equal to that of a circle with radius b^2/a, and a low curvature at its blunt side, corresponding to a circle with radius a^2/b. The curvature of an elliptic leading edge (a laying on the camberline) is therefore initially high, a/b^2, but decreases rapidly and smoothly to its lowest value, b/a^2. The jump in curvature at the tangent point is therefore much lower, as shown in next figure (same scale as Figure 2.1-4). The acceleration and especially the deceleration of the flow around an elliptic leading edge are milder than those observed with a circular leading edge. This keeps the spike in the c_p profile low and helps to avoid the laminar separation.

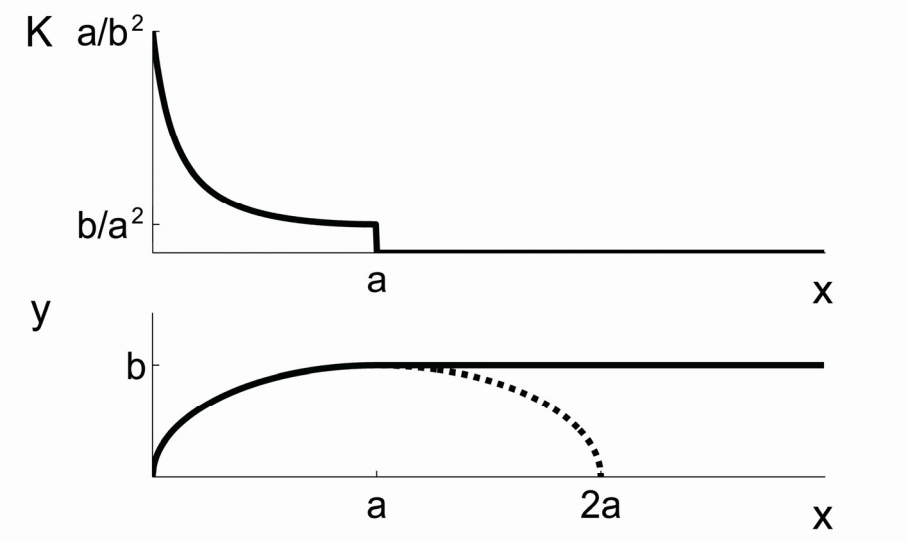

Figure 2.1-5: Curvature of a flat plate with elliptical leading edge

To conclude, a numerical example is given in next figure. On a flat plate, a circular leading edge with radius 1 is compared with an elliptic one having semi-axes 1 and 3.

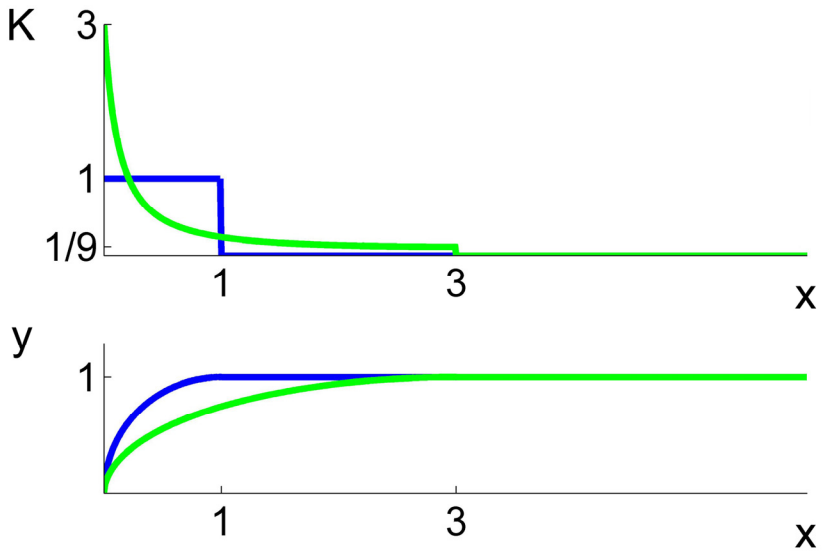

Figure 2.1-6: Circular vs elliptic leading edge

2.1.3 Effect of the Wedge Angle

The size of the c_p spike depends on curvature of the streamline and also on how long this curved path is. A flow particle is forced to follow a curved path from the stagnation point up to the wedge point. It is therefore clear that moving the wedge point toward the stagnation point gives a shorter curved path and a lower spike. The only way to move the wedge point is to increase the wedge angle.

In the example shown in following figure, a flat plate (0° wedge angle) and a profile with 90° wedge angle are compared. In the first case, the curved path is a quarter of the leading edge circumference, in the 90° wedge case, this is only one eighth of the circumference.

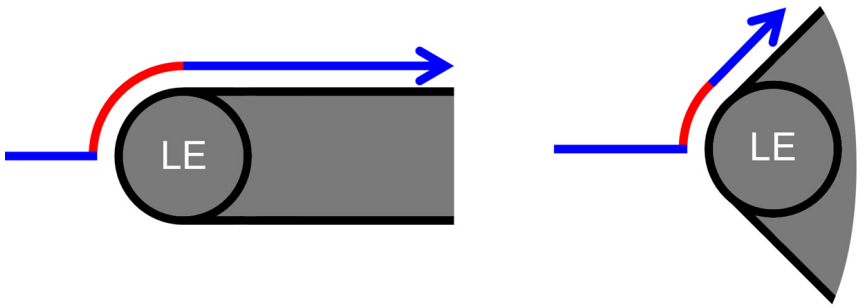

Figure 2.1-7: Streamlines around flat plate and 90° wedge

A high wedge angle is therefore helpful to keep the suction spike low and avoid the formation of a separation bubble.

2.2 LEADING EDGE LOSS

The profile loss of a turbomachinery blade is a function of the momentum thickness at the trailing edge. The momentum thickness θ grows with the boundary layer along the whole profile and depends from the character of the boundary layer and from the initial value θ_0 at the leading edge.

A turbulent boundary layer leads generally to higher loss values. This is because the friction coefficient is lower in a laminar boundary layer. Keeping the boundary layer laminar as long as possible would then lead to lower loss values. On the other hand, a low initial momentum thickness θ_0 is also important to keep the profile loss low. This can be extrapolated from the boundary layer momentum integral equation for incompressible two dimensional flow, in a steady approach and in a similar way to what is presented in [6] and [7].

$$\frac{\partial\theta(x)}{\partial x}+(H+2)\cdot\frac{\theta}{u(x)}\cdot\frac{\partial u(x)}{\partial x}=\frac{c_f}{2} \qquad \textit{Eq. 2.2-1}$$

The skin friction becomes relatively small in the strong adverse pressure gradient. The right hand term is neglected and the equation can be rewritten.

$$\frac{\partial u(x)}{\partial x}<0 \Rightarrow \frac{\partial p(x)}{\partial x}>0 \Rightarrow \frac{c_f}{2}\approx 0 \qquad \textit{Eq. 2.2-2}$$

$$\frac{\partial\theta(x)}{\partial x}\approx -(H+2)\cdot\frac{\theta}{u(x)}\cdot\frac{\partial u(x)}{\partial x} \qquad \textit{Eq. 2.2-3}$$

Some adjustments and integration lead to the following.

$$\int_0^x\frac{\partial\theta(x)}{\theta}\approx\int_0^x-(H+2)\cdot\frac{\partial u(x)}{u(x)} \qquad \textit{Eq. 2.2-4}$$

$$\ln\left(\frac{\theta(x)}{\theta_0}\right)\approx-(H+2)\cdot\ln\left(\frac{u(x)}{u_0}\right) \qquad \textit{Eq. 2.2-5}$$

$$\theta(x) \approx \theta_0 \cdot \left(\frac{u(x)}{u_0} \right)^{-(H+2)} \qquad \textit{Eq. 2.2-6}$$

The momentum thickness at the trailing edge is therefore proportional to that at the leading edge. This means that with a given lift distribution, a small variation in θ_0 is amplified and may lead to a large variation in the trailing edge momentum thickness and in the profile loss.

A separation bubble is likely to be associated with an increase of θ. If the separation can be suppressed, a thinner boundary layer is expected over the whole chord, leading to lower loss values.

As a final comment, an example to show the relevance of this analysis is given. To easily model an airfoil with separation bubble at the leading edge, it is common practice to trip the boundary layer directly at the leading edge assuming the whole flow to be turbulent. This is especially done in CFD, to avoid the problem of modelling the separation bubble. However, this method does not consider the effect of the bubble on the momentum thickness. θ_0 is therefore wrong and the computed loss might be not reliable.

2.3 EFFECT OF WAKES

2.3.1 EFFECT ON INCIDENCE

The incoming flow has a given inlet angle, according to the velocity triangles. When wakes are present, the slip velocity of the wake relative to the free stream changes the inlet velocity triangle, as shown in next figure. This gives a positive incidence on the leading edge, since $\alpha_{1,w} > \alpha_1$.

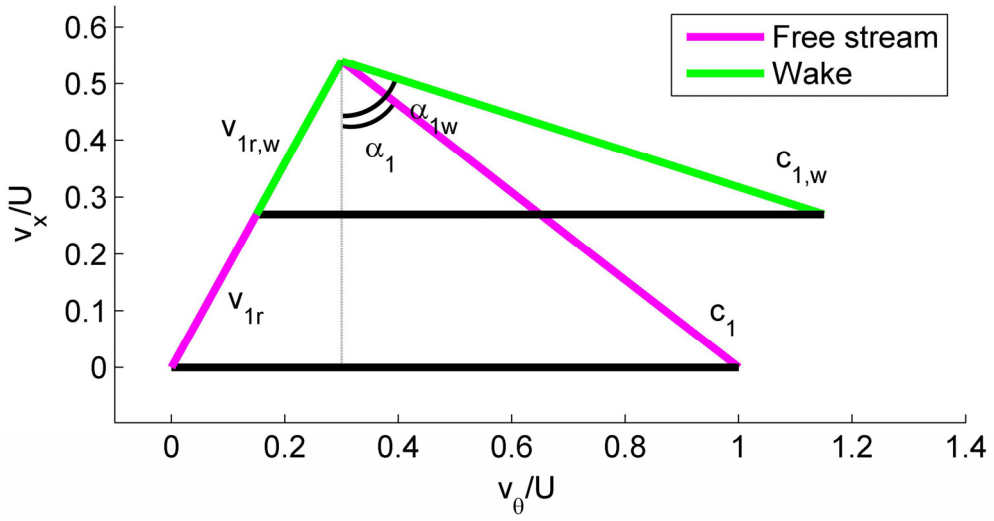

Figure 2.3-1: Stator inlet velocity triangle, with and without wakes

For the same reason, the stagnation point migrates and the local incidence of the stagnation streamline in proximity of the leading edge also varies. As reported in [10], it has been computed that the local incidence of the stagnation streamline is roughly 15° higher at the wake passage.

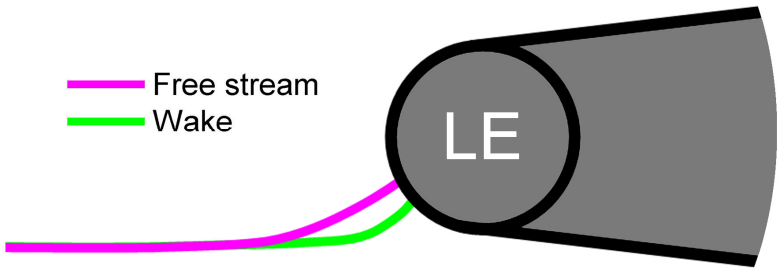

Figure 2.3-2: Stagnation streamline and local incidence

Because of this higher incidence, the flow needs to travel for a longer path around the highly curved leading edge. For this reason, the suction spike in the c_p gets probably higher when the wake passes and the boundary layer properties may vary. It is believed that the transition point on the suction surface migrates toward the leading edge, making a bigger part of the suction side turbulent. On the other hand, where a separation bubble is present, this would probably vary in size, growing when the wake passes. A pulsing behaviour of the separation bubble could be expected. Following a quasi steady approach, according to Eq. 2.2-6, θ_0 and with it the momentum thickness at the trailing edge (and therefore the loss) should also pulse.

2.3.2 WAKE TURBULENCE

The wake is also associated with a higher turbulence level. The measurements reported in [9] show a free stream turbulence level of roughly 2,2% and a value in the wake of 4,5%.

This provides a tool to identify the wakes using unsteady measurement data: the wake should appear as a region of higher turbulence.

2.3.3 WAKE-BOUNDARY LAYER INTERACTION

The interaction between the wake and the boundary layer has been studied in [9] and [10] using particle image velocimetry (PIV) and hot film techniques on the baseline blade. A vortical structure has been measured in the boundary layer. This is induced by the wake and is in phase with it at the leading edge. Then the structure convects on the suction side with a convection velocity that is lower than that of the wake (between 60% and 70% of the wake velocity) and appears delayed at the trailing edge. The momentum thickness measured at the trailing edge shows a peak in phase with this structure, while no appreciable variation could be observed in phase with the wake. It is therefore this wake induced structure, and not the wake itself, to cause perturbations in the boundary layer.

Next figure is a contour plot of normalized vorticity and a vector plot of velocity perturbation taken from [9] (Figure 13). It shows the wake induced structure (marked with P) as a peak of negative vorticity. The wake (marked with W) and its relative slip velocity is also clearly visible.

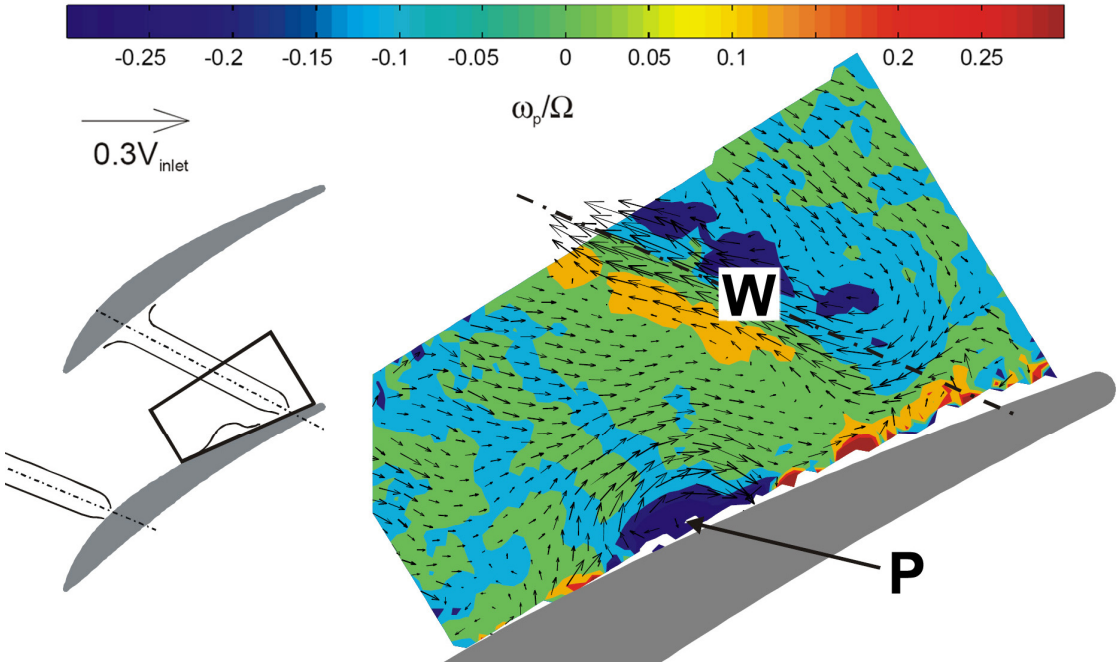

Figure 2.3-3: Velocity perturbation and contours of normalised vorticity

3 BLADE DESIGN PROCESS

3.1 PRELIMINARY STUDY

The wedge angle and the shape of the leading edge have been chosen as design parameters. A series of profiles with different wedge angles and with both circular and elliptic leading edge (3:1 axes ratio) have been designed and their loss coefficient Y_p has been computed with the two dimensional, steady CFD package Mises (see appendix 1).

Y_p is defined as the difference in the mixed averaged total pressure across the stage divided by the inlet dynamic head.

$$Y_p = \frac{p_{tot,out}^{mixed} - p_{tot,in}^{mixed}}{p_{tot,in} - p_{in}} \qquad \textit{Eq. 3.1-1}$$

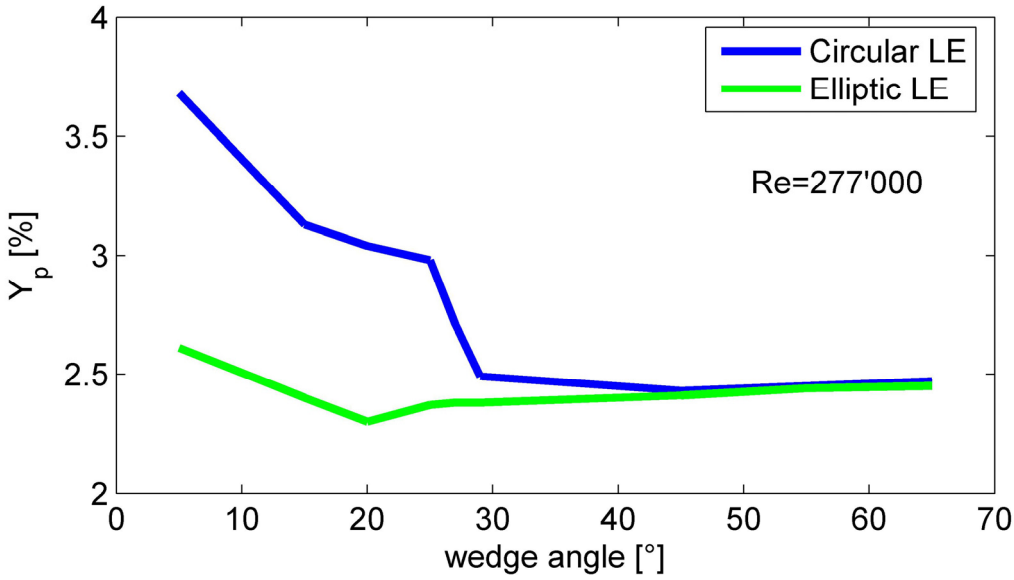

Figure 3.1-1: Loss vs wedge angle, Re=277'000 (based on chord)

This first analysis shows that for wedge angles bigger than roughly 30°, the elliptic and circular leading edge are more or less equivalent. On the other hand, for smaller wedge angles, the elliptic leading edge proves to be much better than the circular one in keeping the loss low. This difference seemed to be associated with the presence of a separation bubble at the leading edge in

case of a circular leading edge with low wedge angle. As explained in 2.1.2, this separation bubble leads in general to worse boundary layer properties and to higher initial momentum thickness θ_0. Higher loss values are therefore expected.

The process of separation and transition is strongly influenced by the Reynolds number. Previous figure shows the results of an analysis conducted at Re=277'000, that is the design Reynolds number of the rig where the reported experiments have been undertaken. Real engine Reynolds numbers can be significantly higher, up to Re=1'800'000. Therefore, the same study has been repeated at higher Re, more representative of real engine conditions.

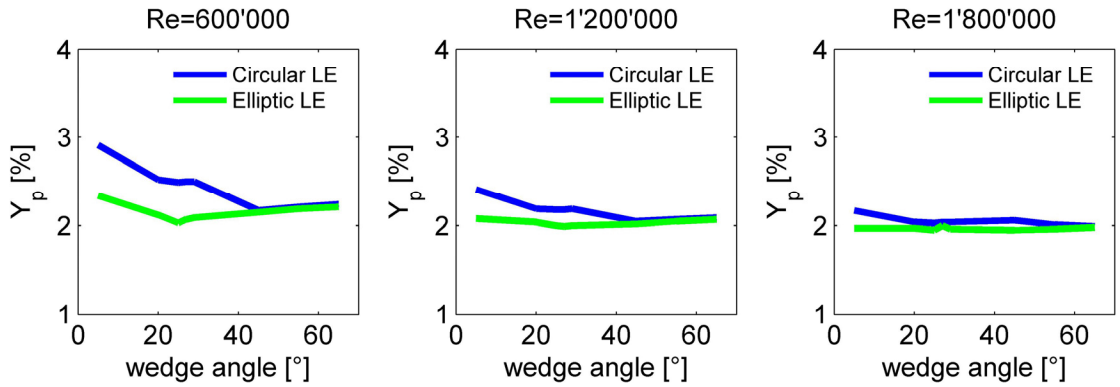

Figure 3.1-2: Loss vs wedge angle, high Re

As expected, the advantage of the elliptic leading edge at low wedge angle drops with increasing Re. This is because at high Re, transition occurs earlier and the separation bubble present on blades with circular leading edge and low wedge angle gets smaller or even disappears. However, even at high Re, the difference in Y_p is still relevant. The advantage of an elliptic leading edge is then significant also in real engine conditions.

3.2 DESIGN GOALS

Goal of this work is to modify the leading edge of an existing blade to test the effects on its performance. For this purpose, the existing blades of the Deverson compressor (see 4.1 and 5.1) have been modified. As explained in the following paragraph, the blades of the Deverson are low speed blades with relatively high thickness to chord ratio (0,1) and high wedge angle (32°). These thick blades are not very representative of the blades of a real engine; real compressor blades are usually very thin. For example, the thickness to chord

ratio of the real blade shown below is roughly 0,05. The wedge angle is therefore low and the blades are similar to thin, flat plates.

Figure 3.2-1: Deverson baseline blade and real engine blade

The first task of the work was therefore to modify the baseline blade so that the new designed blades were more representative of real engine blades. This entails a smaller wedge angle and a reduced profile maximal thickness. The ratio between the leading edge dimension and the chord was also a fixed design constraint and has been chosen to be similar to that of a real, high speed blade. The chord has been kept constant.

Basing on these considerations and on the results presented in 3.1, the following three test cases have been chosen.

Blade A: 32° wedge angle, circular leading edge

Blade B: 15° wedge angle, circular leading edge

Blade C: 15° wedge angle, elliptic leading edge (3:1)

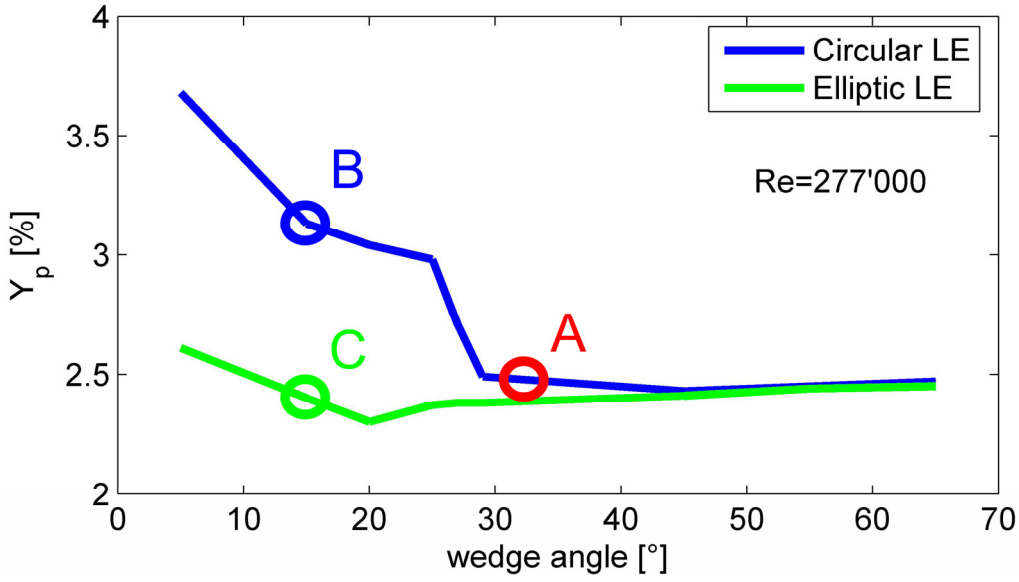

Figure 3.2-2: Test cases

The blade A corresponds to the existing blades of the test rig. Blades B and C are the new designs.

During the experiments, the blade set has not been entirely replaced. For the sake of simplicity and costs only one modified stator blade was used in the baseline set. To keep the aperiodicity as low as possible, the new blades could not be radically different; they should be as similar as possible to the baseline blades. Because the geometry has been changed only close to the leading edge, the aperiodicity is not expected to have large effects.

The final designed blades are therefore very similar to the baseline Deverson blades, except in the region close to the leading edge. The wedge angle has been roughly halved and the leading edge has been thickened. The maximal thickness is only slightly smaller than that of the baseline blades. Finally, two leading edge shapes have been designed: circular and elliptic. Detailed description of the new builds is given in chapter 4.

3.3 DESIGN PROCESS

3.3.1 GEOMETRY MODIFICATION

The geometry of the three-dimensional blades is defined at 21 sections. The coordinates are stored in cylindrical coordinates r–θ–z in a blade definition file.

A Matlab script has been used to modify the blade geometry. The routine reads the coordinates of each section from the blade definition file of the baseline blade, computes the camberline and the thickness distributions of both suction and pressure side, calls a subroutine to modify the thickness distributions at the leading edge and reconstructs the airfoil from the camberline and the new thickness distributions. Finally the new coordinates are written in a new blade definition file.

The thickness distribution is modified according to following procedure. First of all the new leading edge shape (a circle or an ellipse of given dimension) is imposed and the wedge point is set. Its position is univocally fixed by the chosen wedge angle; the wedge point is by definition the point where the leading edge is tangent to the line having the slope equal to the tangent of the wedge angle.

Then, a cut point on the blade surface must be chosen and finally a curve must be fitted between the cut point and the wedge point. A Bézier curve has been chosen for this purpose.

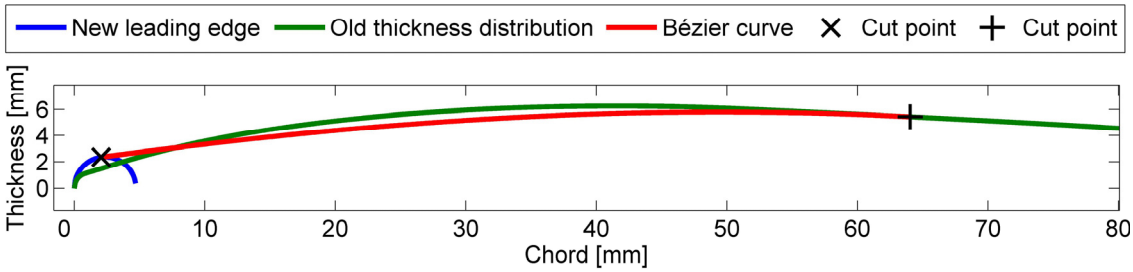

Figure 3.3-1: Modified thickness distribution

3.3.2 MISES AS A DESIGN TOOL

As explained in 3.2, the geometry of the new designed blades and the flow field around them should be as similar as possible to the baseline blade. To check the agreement between the different flow fields, Mises has been run on each new designed profile and the new c_p distribution has been compared with the baseline. The design process was therefore a strongly iterative procedure, where efforts have been made to understand the effect of geometrical constraints like the position of the cut point and the properties of the Bézier curve.

Intuitively, since the airfoil is only modified from the leading edge to the cut point (where the curve is fitted), it can be supposed that the cut point should be set in proximity of the leading edge. However, since the size of the leading edge and the wedge angle are radically different, Mises results showed that a smooth Bézier curve and a c_p profile without singularities cannot be achieved if the cut point is set too near to the leading edge.

As a good compromise, the position of the cut points of the new blades varies spanwise between 50% and 60% of the chord.

A description of the new designed profiles and a comparison of the computed c_p distributions are given in chapter 4.

3.4 CONSTRUCTION DETAILS AND MANUFACTURING

3.4.1 MANUFACTURING PROCESS

The blades have been built with a stereolithography process. Stereolithography (SLA) is a rapid prototyping process that produces plastic parts solidifying a liquid photopolymer using a laser beam. When the beam hits the free surface of the liquid it solidifies the resin and when a layer is fully traced the elevator in the vat is slightly lowered, sinking the model. Then the laser starts tracing the next layer. The material is self-adhesive and the layers stick with each other. Layer by layer, a full three-dimensional part is formed directly from the CAD model.

This manufacturing process is quick, simple, relatively cheap and, above all, it allows the production of rather complicated geometries like instrumented blades with internal cavities. On the other hand, only a narrow range of materials can be used for stereolithography. Anyway, from the point of view of mechanical stress, the stator blades of a low speed rig like the Deverson (see chapter 5) don't experience difficult conditions and don't present particular issues. The resin used by the SLA process is therefore well suited for this application.

The tolerances of this rapid prototyping process are on the order of 0,1 mm, that is accurate enough for this purpose. However, to ensure good results, wall thicknesses and tappings diameters below 1 mm should be avoided. Because of the layer-by-layer building process, the raw parts have slightly rough surfaces; some hand polishing is needed.

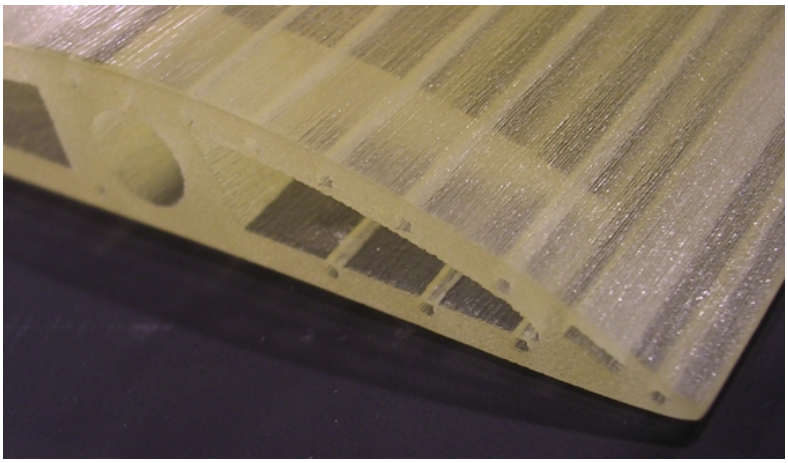

Figure 3.4-1: Baseline blade, detail of the tip surface and leading edge, unpolished

3.4.2 PRESSURE TAPPINGS

As presented in paragraph 6.1, time averaged measurements of the c_p distribution on both blade surfaces have been taken. For this purpose, the test blades had to be instrumented with a number of pressure tappings. These are actually thin tubes situated just below the surface, connected at one side to pressure sensors and closed at the other side. The blade surface has been drilled at mid-height in correspondence of each tapping, opening it and allowing the measurement of static pressure. The biggest pressure gradients are expected to be on the suction side; a finer resolution is therefore wanted on that side and the tappings are more densely distributed.

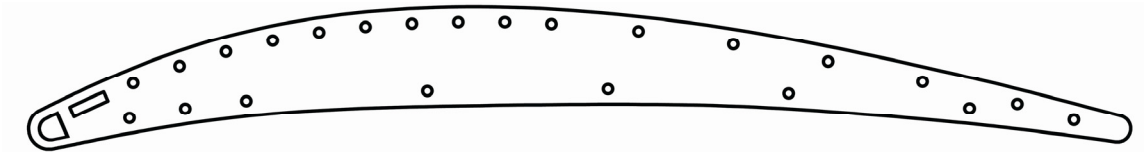

Figure 3.4-2: Pressure tappings and cavities, blade B, mid span

As showed in the figure, larger cavities have been designed in the region of the leading edge and the surface has been drilled in many points, in a “pepper pot” manner. A pricked tape was then used to cover all the holes except one. This allowed a much finer resolution around the leading edge. In order to keep the blade as strong as possible to avoid any kind of deformation during the experiments, the large cavity at the leading edge does not run through the whole blade. It is actually a chamber positioned at mid-height and it is 20 mm long spanwise.

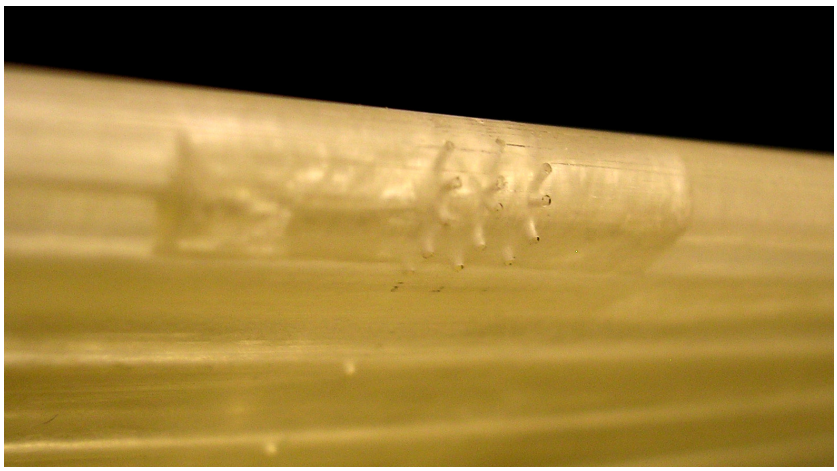

Figure 3.4-3: Blade B, internal cavity and “pepper pot” leading edge

Unfortunately, it was impossible to design a cavity at the leading edge on the baseline blade, due to the small size of the leading edge and to the constraints given by the manufacturing process used (see 3.4.1). In that case a slot crossing the tapping has been cut and the pricked tape has been used again.

3.4.3 FIXING TO THE RIG

The blades are equipped with an M6 threaded bush at the tip surface to be fixed to the casing of the compressor.

Near the tip surface, all tappings are connected to thin plastic tubes. These pass through two further holes in the casing and reach the pressure sensors. To ensure enough room for such connections, a large cavity has been designed at the tip surface of the blades (see Figure 3.4-1). Following figure shows a finished blade, ready for the rig.

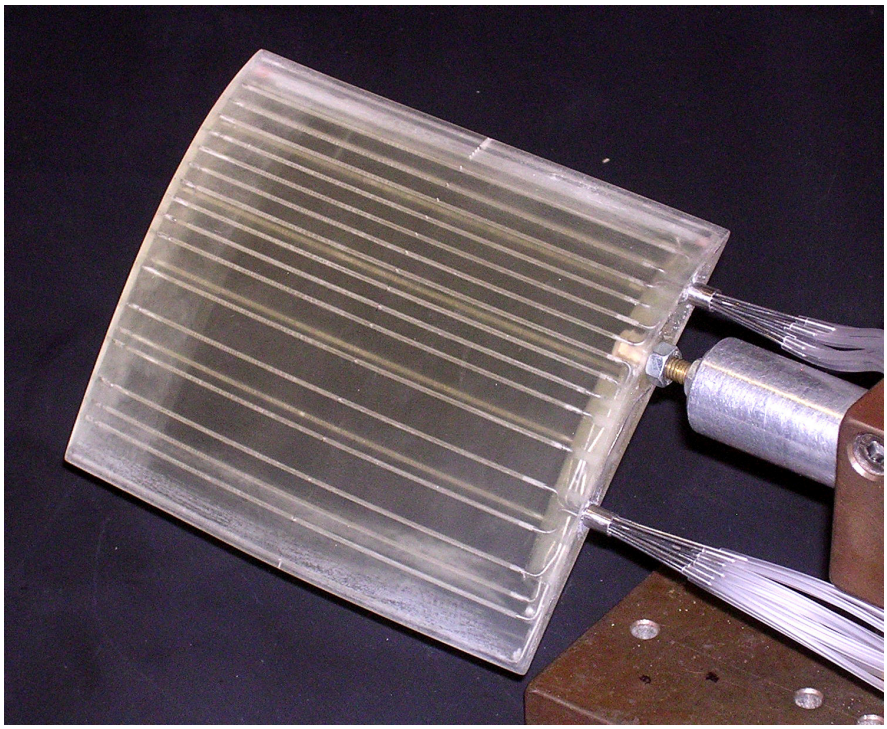

Figure 3.4-4: Baseline blade fully instrumented

4 TEST GEOMETRIES AND CFD ANALYSIS

4.1 BLADE A (DEVERSON BASELINE BLADE)

The blade A is the baseline stator blade of the rig. Its design was not part of this work, the geometry is described in [2] as the build 2. The leading edge is circular with 2,3 mm diameter. The wedge angle is 32°. At mid-height, the inlet metal angle is 52,3° and 25,0° is the exit one, as given in next figure. The true chord is 126 mm and 74,4 mm is the axial chord.

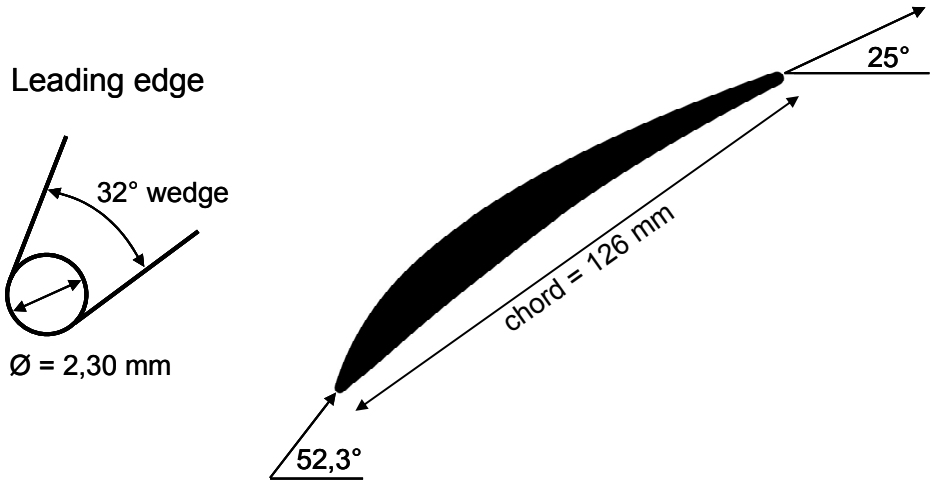

Figure 4.1-1: Baseline geometry, mid-height

The mid-height profile has been investigated using Mises, giving the profiles of the pressure coefficient c_p, shape factor H and friction coefficient c_f shown in Figure 4.1-2. Mises has been run at the same conditions of the rig. The inlet velocity and the mass flow have been set to mach the design flow coefficient of the rig of 0,51, the inlet flow angle is 52,3° (corresponding to an inlet slope S_1 of 1,29), the turbulence level 2,74% (time mean of the values reported in [10], see 2.3.2).

The computed loss coefficient Y_p is 2,38%

A suction spike at the leading edge is present. It is relatively small and the downward side does not present any kink. This suggests that the boundary layer stays laminar and does not separate.

The shape factor of the suction side is initially 2,5, then has a peak at about 20% of the chord and drops subsequently to 1,7. The peak in H is the transition point. As the shape of the leading edge spike suggested, Mises predicts a laminar boundary layer up to 20% chord and a turbulent one afterwards. A kink is also present in the c_p profile at the same position.

c_f does not reach zero at any point. This means that no separation is present. This is particularly important at the leading edge and is consistent with the remarks above: if a separation bubble at the leading edge was present, the boundary layer would have been turbulent from the beginning. The very high peaks in the c_f distribution at the leading edge correspond to the stagnation point, where the stagnation streamline impinges.

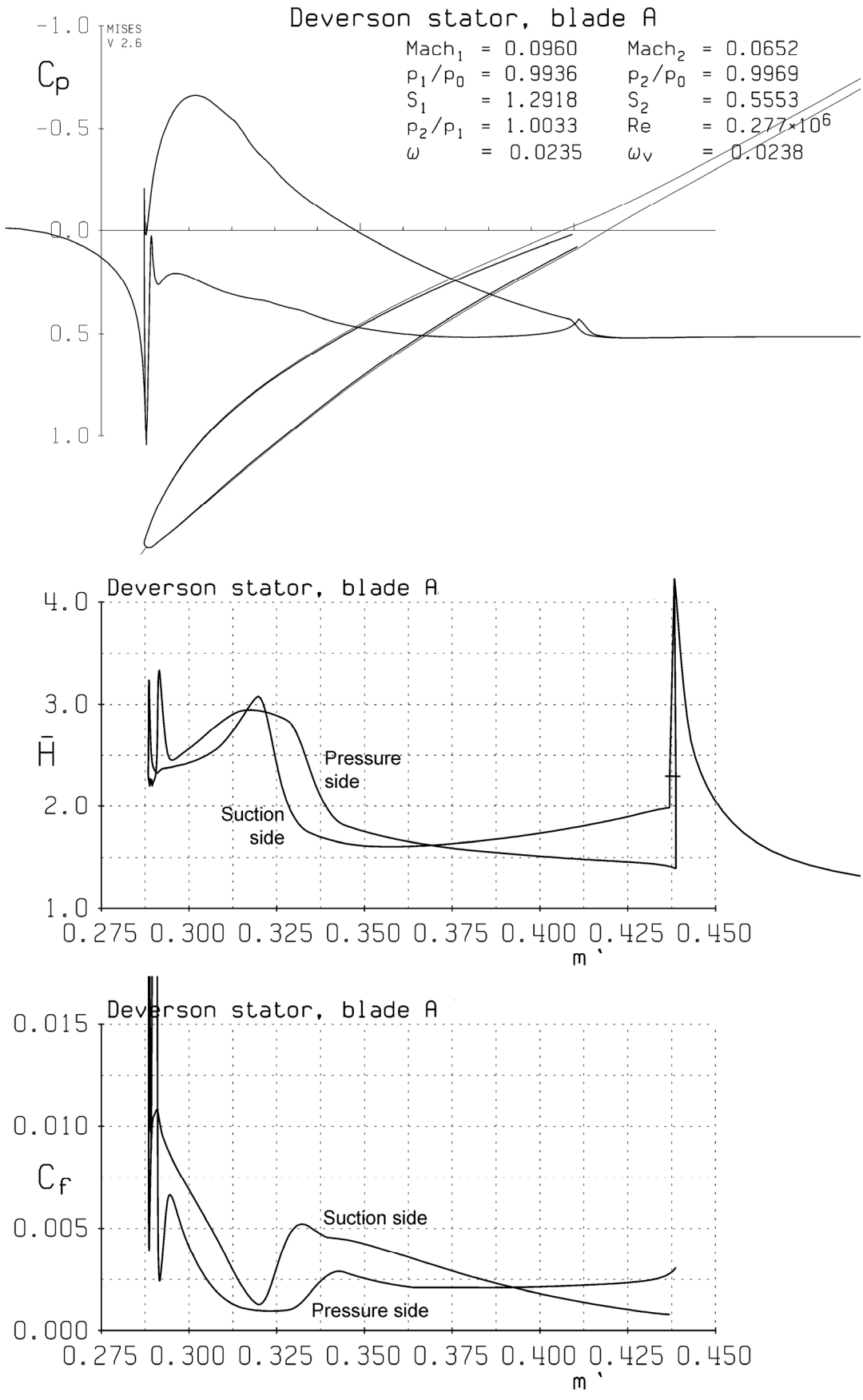

Figure 4.1-2: Mises analysis of blade A

4.2 BLADE B

The blade B has a thick, circular leading edge. The leading edge diameter is 4,72 mm and the wedge angle is 15°. The blade has been built starting from the baseline geometry according to the procedure explained in chapter 3. The camberline has not been modified and the metal angles are therefore the same. The geometry of the mid-height airfoil is shown in next figure.

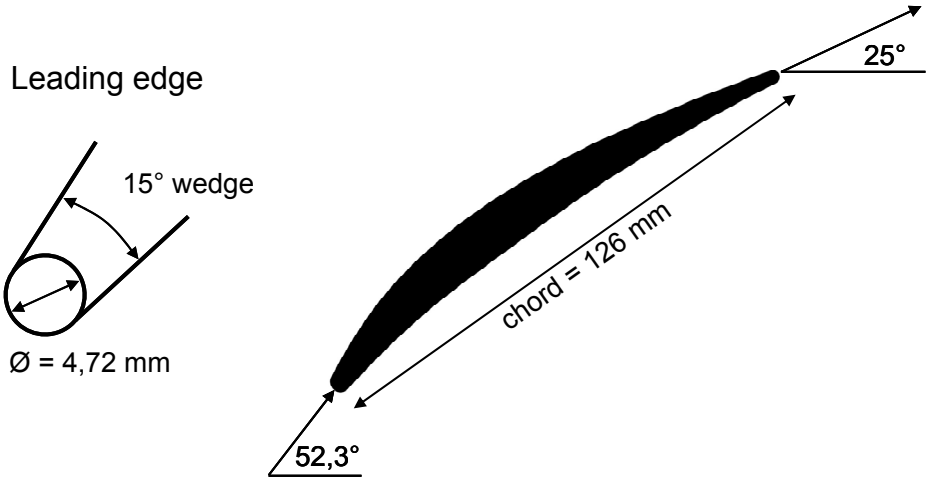

Figure 4.2-1: Geometry of blade B, mid-height

Mises has been run on this blade at the same conditions and at mid-height, with the results shown in Figure 4.2-2.

The biggest difference is the much higher leading edge spike at the leading edge on both surfaces, due to the different geometry. A kink on the downhill side of the spike is visible, revealing the presence of a separation bubble. The peak suction point is also slightly lower than on blade A (more details in 4.4).

The H profile shows a high and sharp peak near the leading edge, at the wedge point. It corresponds to the separation bubble. Afterwards, the reattached boundary layer is fully turbulent and the value drops immediately to 1,7.

The friction coefficient goes to zero near the leading edge, proving definitively the presence of a separation bubble.

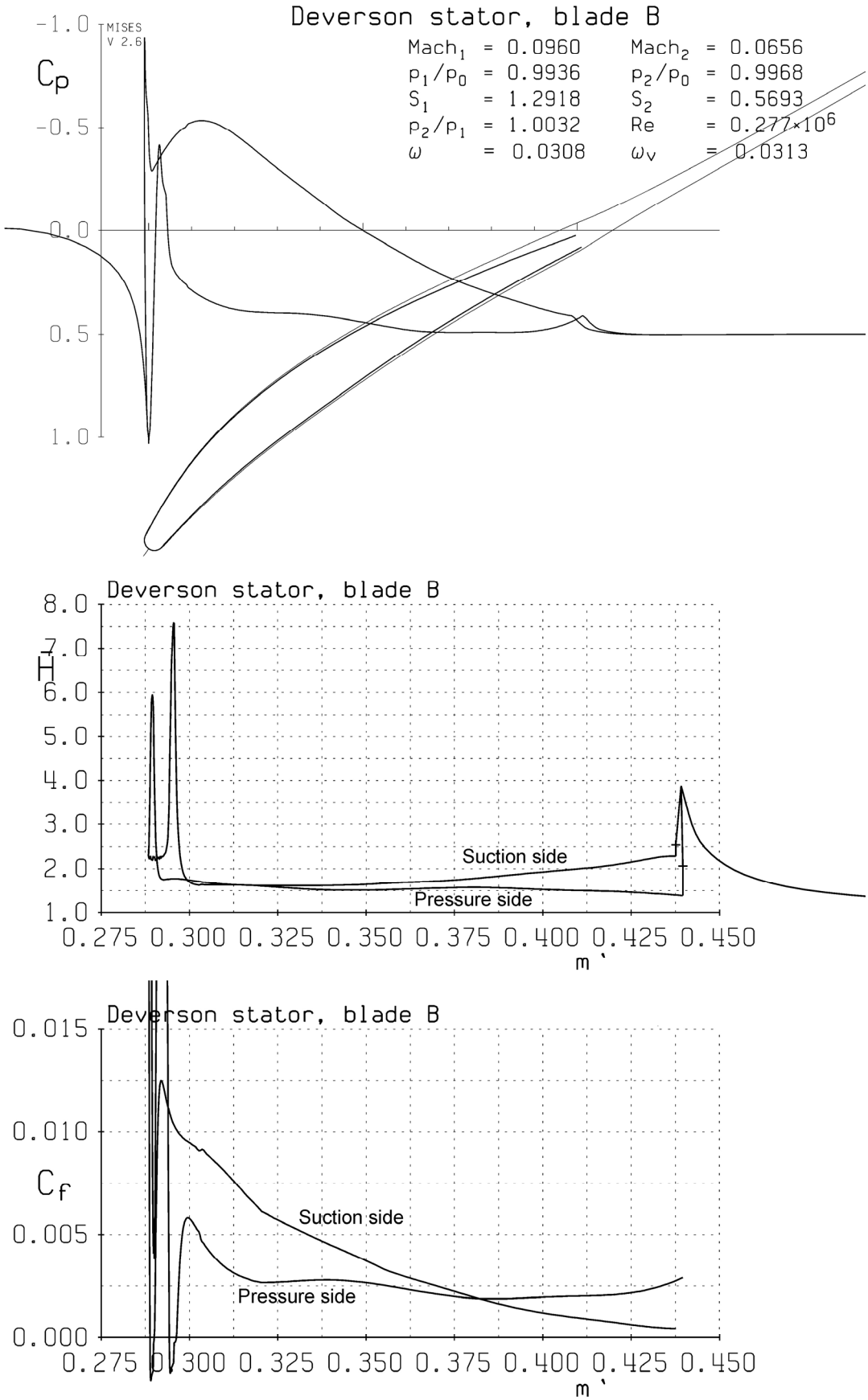

Figure 4.2-2: Mises analysis of blade B

4.3 BLADE C

The blade C is based on blade B; the blades are perfectly the same, except the shape of the leading edge, which is now elliptic with the axes ratio being 3:1. The wedge angle is again 15°.

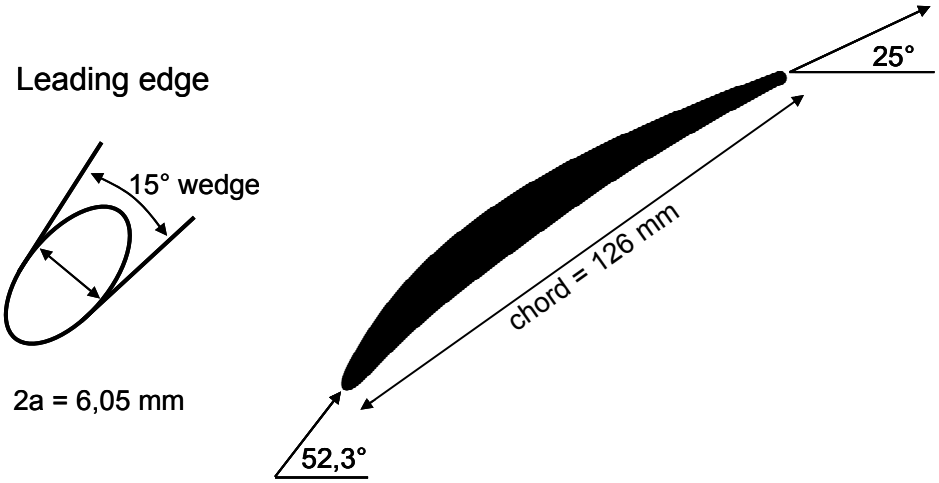

Figure 4.3-1: Geometry of blade C, mid-height

Mises applied on this geometry gives the results plotted in Figure 4.3-2.

The suction side c_p is very similar to blade B, except near the leading edge spike. The elliptic leading edge makes it almost disappear and part of the boundary layer can be assumed to be laminar. A kink can be observed again after the peak suction point, showing probably the transition point.

The H profile of the suction surface is similar to the profile computed for the baseline blade. A similar interpretation leads to the conclusion that the boundary layer is laminar for roughly 20% of the chord and turbulent afterward. On the other hand, the H spike on the pressure surface appears to be near the wedge point, suggesting the presence of a separation bubble on the pressure surface. However, the height of the spike (3,75) is relatively low, much lower than those found at the wedge points of blade B (6 on the suction side ant 7,5 on the pressure side). The friction coefficient at that point is also very low, but not zero. It is therefore difficult to predict if the flow really separates at the wedge point on the pressure surface. In any case, the H value shows the turbulent character of the boundary layer downstream the wedge point.

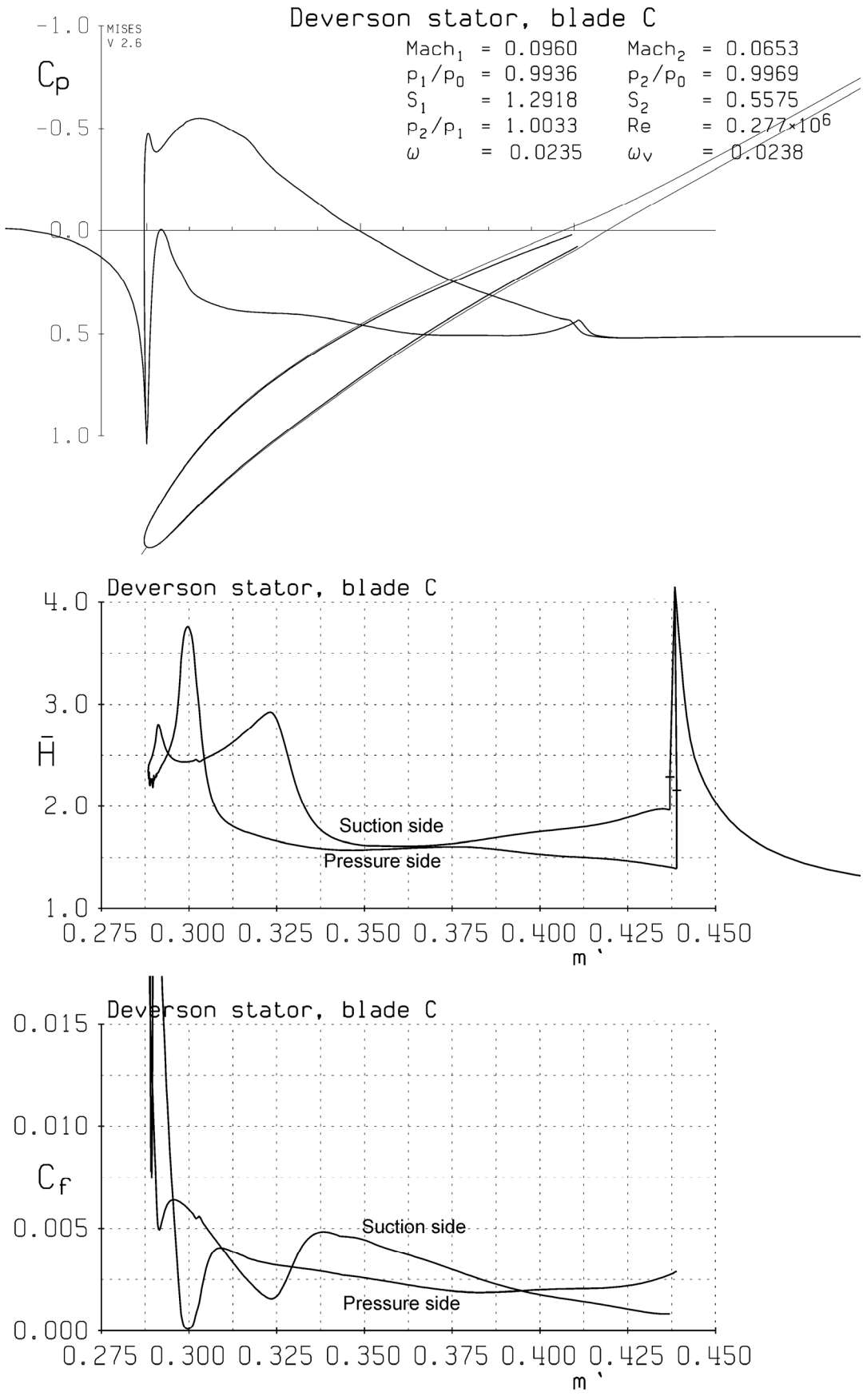

Figure 4.3-2: Mises analysis of blade C

4.4 COMPARISON

In next figures, the mid-height profiles of blades A and B are drawn together, and the c_p distributions are superimposed. This direct comparison shows the effect of the wedge angle variation. As explained in 2.1.3, where the wedge angle is high, the path around the leading edge circle is shorter. The flow is less accelerated and the leading edge peak is lower.

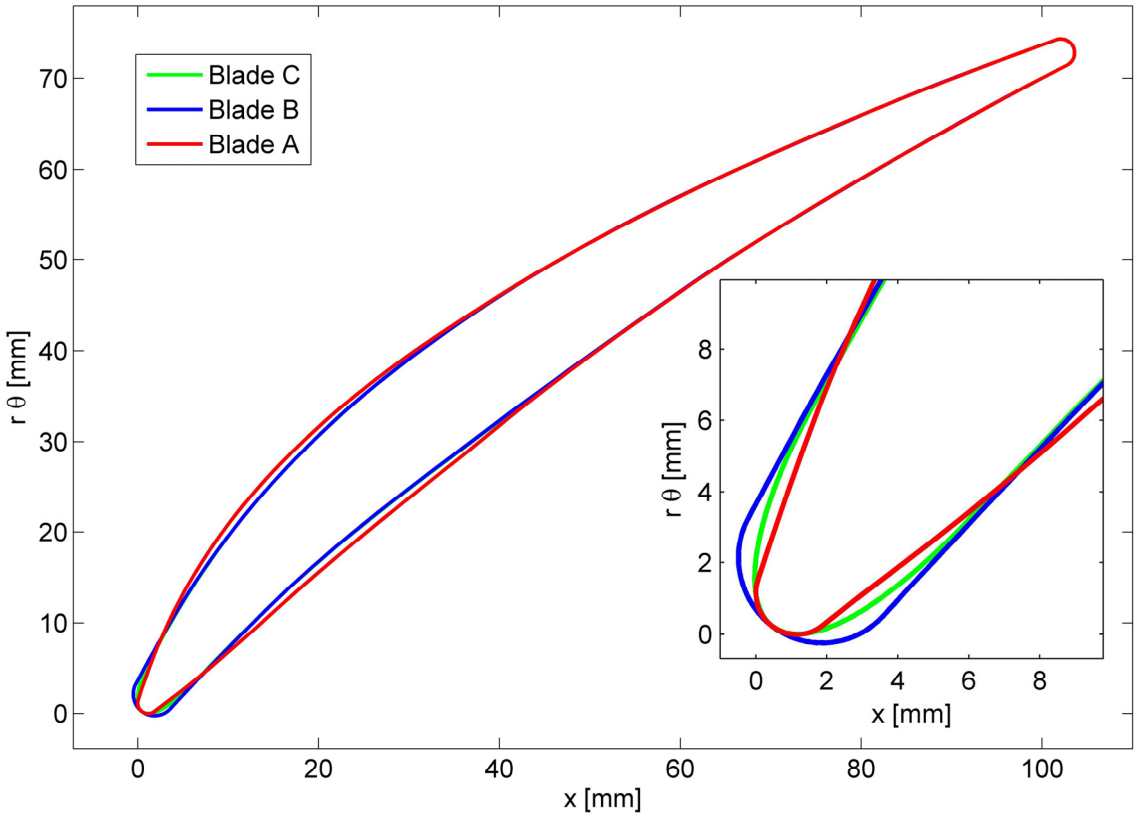

Figure 4.4-1: Mid-height blade profiles

The difference in the peak suction and generally in the whole c_p profile is likely to cause some aperiodicity in the rig, since only one blade has been replaced. The peak suction is lower because the modified blade is thinner and its curvature at the throat is lower. The designed profiles are the results of an iterative process which aimed to obtain a c_p distribution as similar as possible to the baseline one. However, it was not possible to build a blade with exactly the same c_p distribution (except at the leading edge) as the baseline one, with such deep modifications in the leading edge dimensions and in the wedge angle; especially considering that most of the geometrical constraints were more or less fixed. In any case, the results of this work are believed to be only

slightly affected by the aperiodicity and no change in the conclusions is expected.

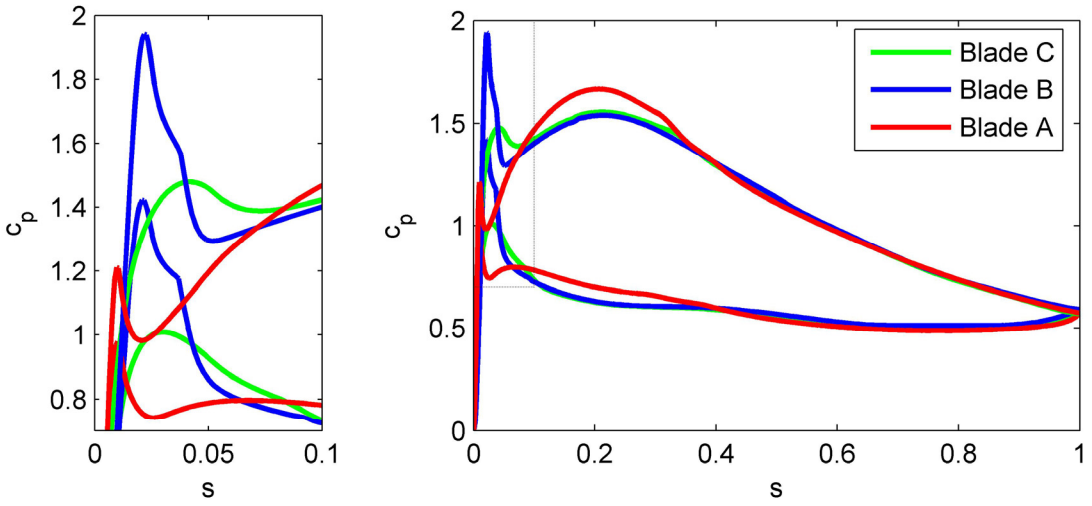

Figure 4.4-2: Computed c_p distribution, all blades

A direct comparison between blades B and C shows the effect of the different leading edge geometry on the suction spike. As expected, the c_p distribution is the same but the suction spike with the elliptic leading edge is much lower and no separation is present. This is in agreement to the consideration given in 2.1.2.

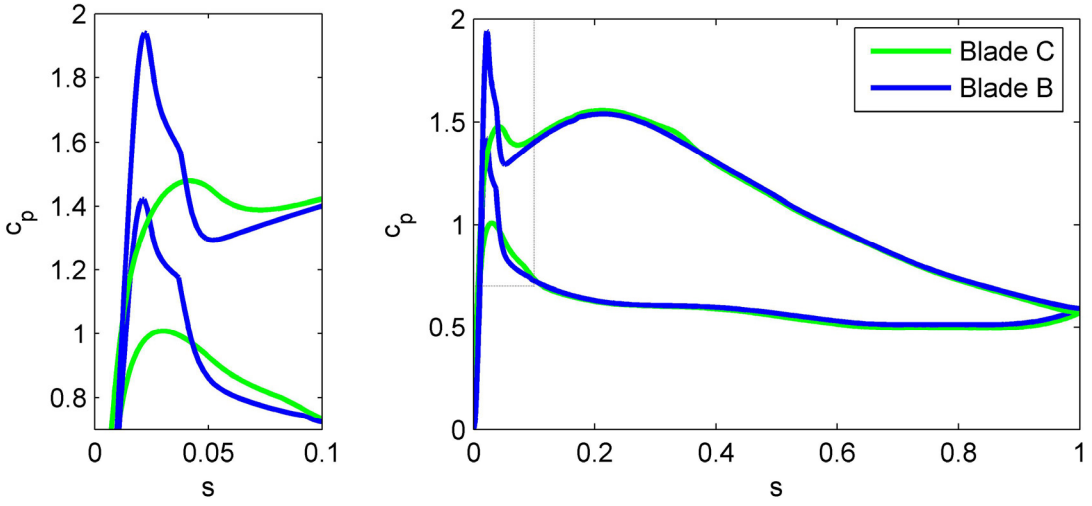

Figure 4.4-3: Computed c_p distribution, blades B and C

5 EXPERIMENTAL APPARATUS AND TECHNIQUES

5.1 THE DEVERSON RIG

5.1.1 OVERVIEW AND DESIGN CONDITIONS

The Deverson Rig at the Whittle Laboratory is a single stage, axial flow, low speed compressor. The rig was completed in 1965 and has undergone several modifications since. The most important features of the Deverson compressor are summarized in the following paragraphs; for any further detail it is here remanded to [2] and [4], where the rig is deeply described.

For the experiments of this work, the rig has been run at the design conditions of 500 rpm rotor speed, flow coefficient $\varphi = 0{,}51$ and Reynolds number Re=277'000 (based on the blade chord).

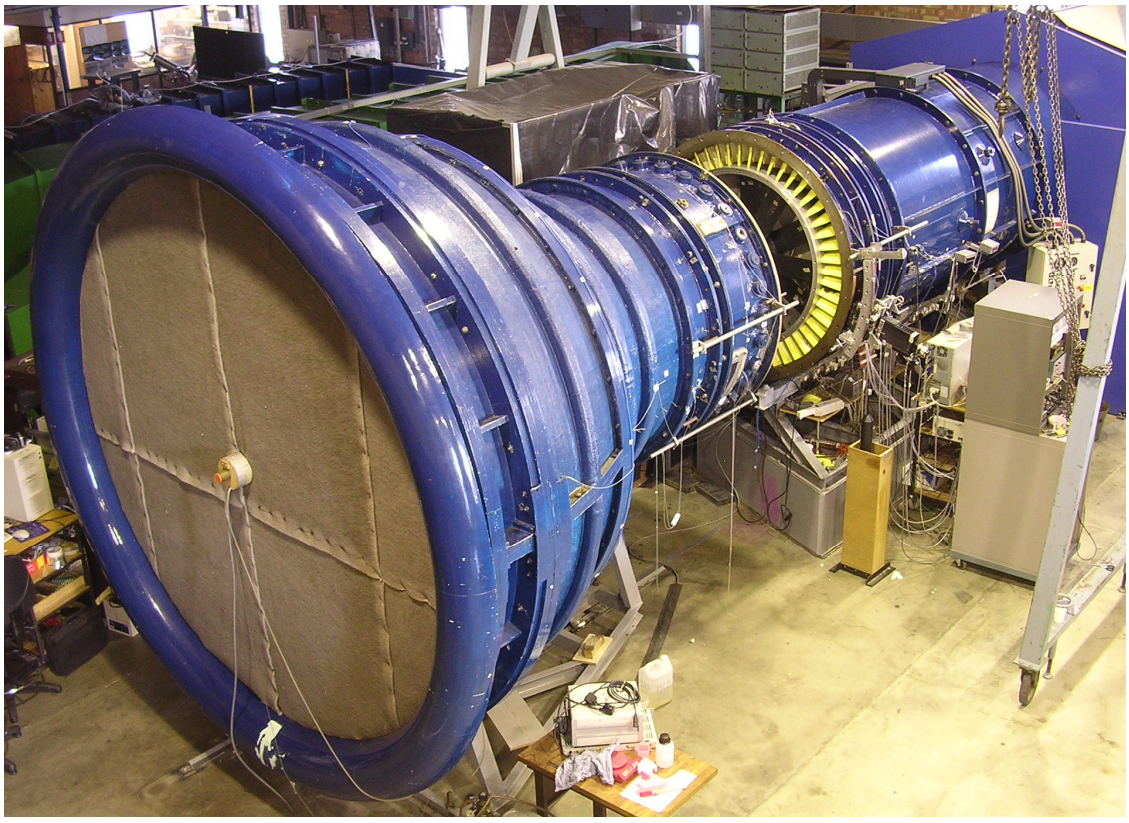

Figure 5.1-1: The Deverson rig (split), inlet diameter 2,8 m

5.1.2 GEOMETRY AND FLOW PATH

The flow enters through a filter to remove dirt and then passes through honeycomb sections to be straightened. After a 9,3 to 1 area contraction the air passes into a parallel annulus of 152,4 mm height (1,524 m tip diameter and 0,8 hub to tip radius ratio) and approximately eight axial chords in axial length, where the inlet guide vanes and the research stage are situated. The annulus remains cylindrical for roughly 15 axial chords downstream of the stage, and then the flow goes through a dump diffuser and a conical throttle valve. From there the air enters the centrifugal auxiliary fan and finally exhausts to the atmosphere.

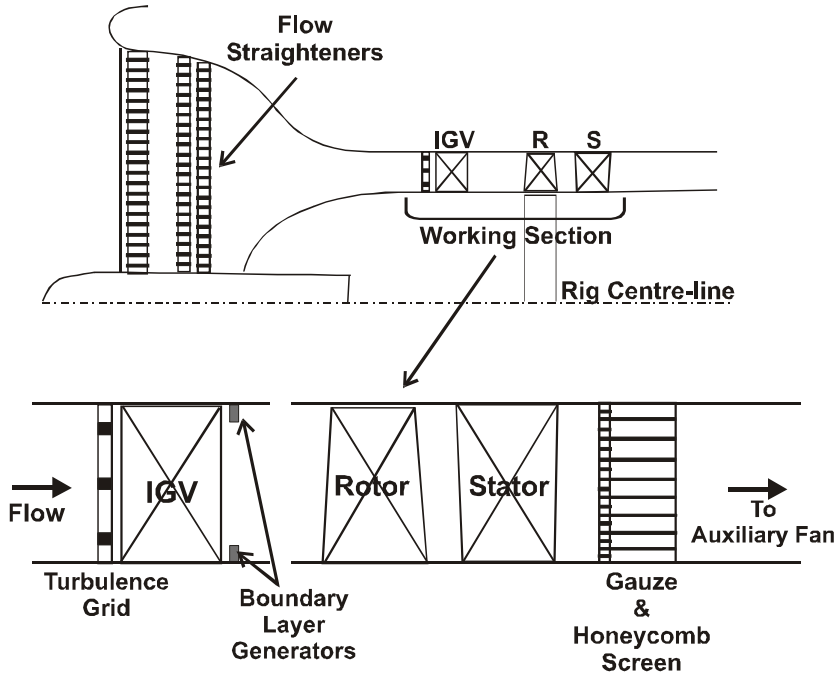

Figure 5.1-2: Meridional view of the Deverson rig

The research stage is formed by a rotor with 51 blades followed by a stator with 49 blades. The pitch to chord ratio at mid-height is 1,18 (103,6 mm axial chord and mid-radius of 685,8 mm). The blades geometry is described in [2] as the build 2, the velocity triangles are plotted in next figure.

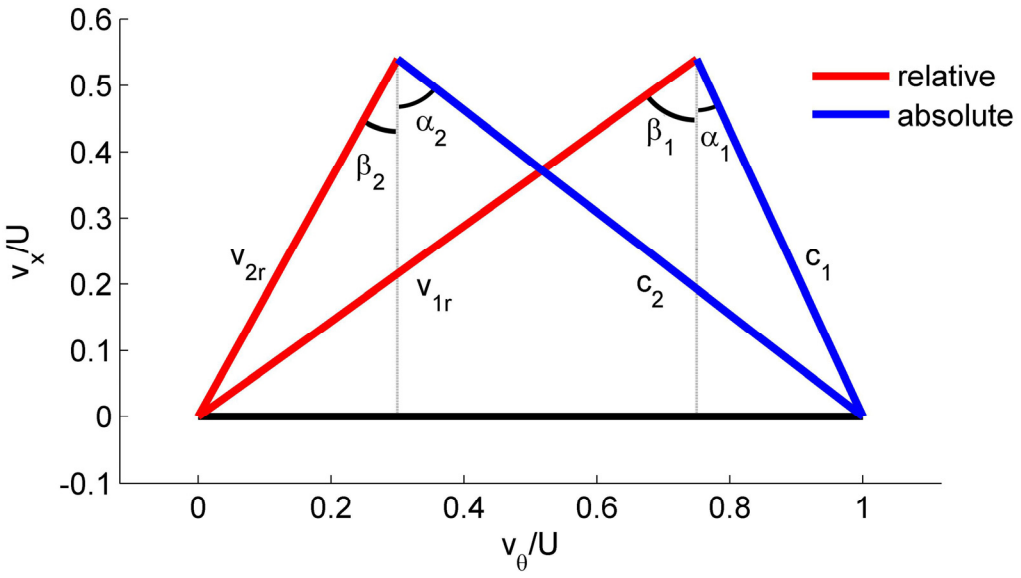

Figure 5.1-3: Velocity triangles

5.1.3 A MULTI STAGE ENVIRONMENT IN A SINGLE STAGE RIG

To make the flow field in the Deverson single stage compressor representative of an embedded stage, some features of the multi stage environment are reproduced in the rig.

Upstream the test rotor, rows of metal teeth are fitted to the casing and the hub to thicken the oncoming boundary layers and simulate the typical axial velocity profile experienced by an embedded stage. To bring the turbulence level and its length scale nearer to those of a multi stage machine, a turbulence grid has been placed just upstream the inlet guide vanes.

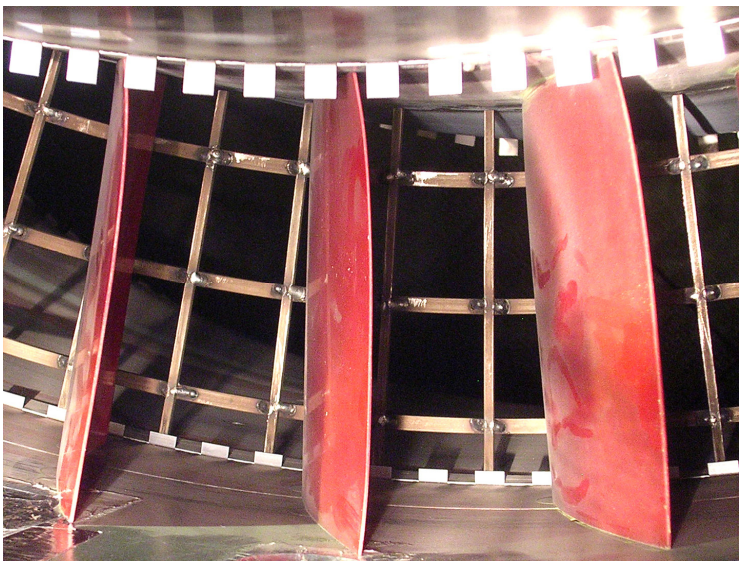

Figure 5.1-4: Inlet guide vanes, turbulence grid and boundary layer thickeners

Since the flow of a compressor stage is also affected by the potential field of the downstream stage, a pressure-loss screen and honeycomb was installed downstream the rotor to simulate the effect of the downstream stage.

An auxiliary fan is placed far downstream the research stator. This fan provides additional pressure rise to draw the flow through the compressor and allows the flow rate to be altered independently of the research rotor speed.

5.1.4 DATA ACQUISITION AND INSTRUMENTATION

Slots in the casing allow traversing of probes upstream and downstream the stator of the research stage. An external traversing system, controlled by a personal computer with LabVIEW user interface, provides three axis motion for probes (radial and circumferential positioning and yaw angle).

Two pressure tappings are situated on the casing before and after the area contraction. These signals (p_{A1} and p_{D2} respectively) are used to evaluate the flow coefficient and to normalize the experimental data as explained in 5.2.

For time averaged pressure measurements, a digital pressure transducer with his own IP address is used. Hot wire bridges (see 0) are also connected to the pc through a NIdaq board for time resolved velocity measurements. LabVIEW programs manage the data logging and Matlab scripts are used for the off-line post-processing.

5.2 c_P MEASUREMENTS

As explained in paragraph 3.4.2, a number of pressure tappings have been designed in the test blades and each tapping has been drilled at mid-height and connected through plastic tubes to the pressure transducer. This allows the measurement of the static pressure in correspondence of each tapping and the evaluation of the non dimensional pressure coefficient c_p.

Some difference of the running conditions between different runs must be taken into account. Before computing the pressure coefficient, the measured pressure has been corrected as follows: the raw measured pressure p_{raw} is non dimensionalised with the actual p_{A1} and p_{D2} (see 5.1.4), then the corrected pressure p is evaluated using some reference p_{A1}^{ref} and p_{D2}^{ref}, corresponding to the reference running conditions.

$$c_p^{raw} = \frac{p_{A1} - p_{raw}}{p_{A1} - p_{D2}} \qquad \textit{Eq. 5.2-1}$$

$$p = p_{A1}^{ref} - c_p^{raw} \cdot \left(p_{A1}^{ref} - p_{D2}^{ref}\right) \qquad \textit{Eq. 5.2-2}$$

Using this corrected pressure the pressure coefficient c_p can be computed.

$$c_p = \frac{p_{tot,in} - p}{p_{tot,in} - p_{in}} \qquad \textit{Eq. 5.2-3}$$

Thanks to the pressure correction, the results are very accurate and repeatable. The biggest difference in the c_p measured from the same tapping in different runs in c_p was only about 0,02 (between 1,5 and 4%).

5.3 OIL & DYE FLOW VISUALIZATION

The oil & dye technique is an extremely simple but very useful qualitative flow visualization technique. The blades are painted using a mixture of silicon oil and fluorescent pigment and the rig is run until the paint dries out. With the help of a ultra-violet lamp, the streamlines can be observed and phenomena like separated regions are clearly visible. Moreover, the intensity of the pigment gives an indication of the magnitude of the friction coefficient on the blade surface.

5.4 THREE-HOLE PROBE MEASUREMENTS

5.4.1 INTRODUCTION

A three hole probe has been traversed 0,3 axial chords downstream of the trailing edge of the modified blades, covering half a passage above and below the test blade. This allowed the measurement of the time averaged pitchwise total pressure profiles and to compute the loss.

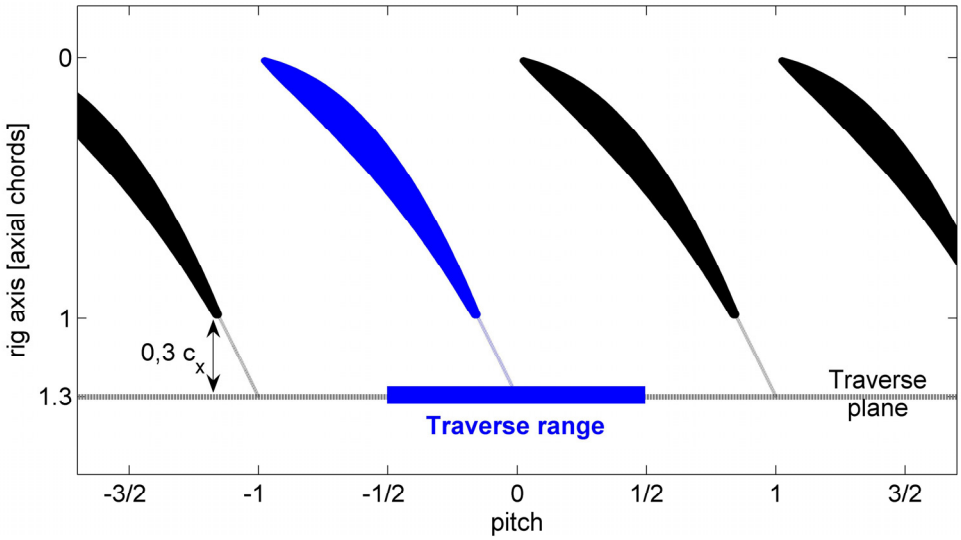

Figure 5.4-1: Traverse range

The use of the three hole probe implies the assumption of a two dimensional flow field. This is consistent with the rest of the analysis.

5.4.2 PROBE GEOMETRY AND OPERATING PRINCIPLE

A three-hole probe consists on a bundle of three thin tubes whose tips are manufactured with different orientation. The tube tips lay one upon the other, in the same meridional plane. The probe is inserted radially into the rig and its head is cobra-neck shaped.

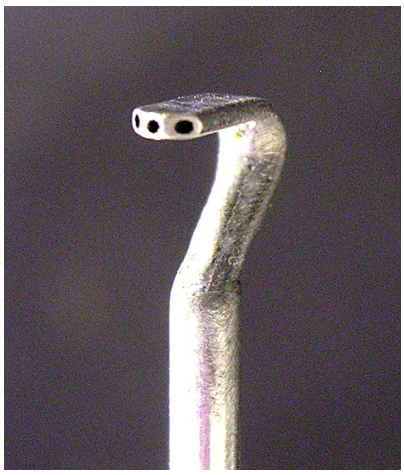

Figure 5.4-2: Detail of the tip of the used three-hole probe

Because of the manufacturing of the tip of the probe, each tube measures the same static pressure (assuming negligible size) but a different dynamic head, which is proportional to the square of the velocity component perpendicular to the tip surface (red arrows in next figure). This allows the evaluation of all needed flow data such as yaw angle, velocity, static and total pressure.

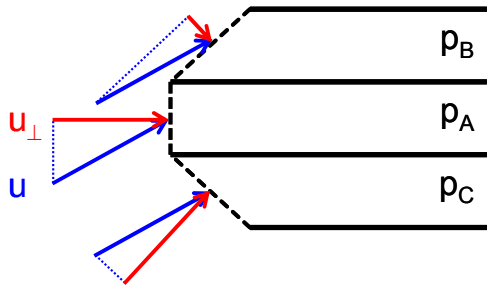

Figure 5.4-3: Schematic of three-hole probe measuring principle

5.4.3 PROBE CALIBRATION

The probe has been calibrated in a separated calibration tunnel equipped with a pitot probe, where the flow direction is known. The procedure is similar to that used in [10]. During the calibration session the probe is yawed across the wanted calibration range (±30°). Three non dimensional parameters are built with the three pressure signals measured by the probe and the total and static pressure taken from the pitot probe: yaw coefficient C_{yaw}, stagnation coefficient C_{stag} and dynamic head coefficient C_{dyn}.

$$C_{yaw} = \frac{p_B - p_C}{p_A - \left(\frac{p_B + p_C}{2}\right)}$$ *Eq. 5.4-1*

$$C_{stag} = \frac{p_{tot} - p_A}{p_A - \left(\frac{p_B + p_C}{2}\right)}$$ *Eq. 5.4-2*

$$C_{dyn} = \frac{p_{tot} - p_{stat}}{p_A - \left(\frac{p_B + p_C}{2}\right)}$$ *Eq. 5.4-3*

Three calibration curves are drawn: the yaw angle, C_{stag} and C_{dyn} are plotted against C_{yaw}. The curves are then smoothed through a high order polynomial fit. These polynomials are used to evaluate the flow data (flow angle, total and static pressure) according to following procedure. p_A, p_B and p_C are measured and C_{yaw} is built from it. The calibration polynomials give the yaw angle and the coefficients C_{stag} and C_{dyn} corresponding to the measured C_{yaw}. Finally, the total and static pressure are extrapolated from C_{stag} and C_{dyn} respectively.

5.4.4 DATA ACQUISITION AND POST PROCESSING

The movement of the traverse gear, the acquisition of the pressure signals and the rig monitoring are managed by a LabVIEW program. The same correction presented in 5.2 has been applied to the pressure signals to remove the effect of fluctuations in the running conditions.

The loss coefficient Y_p is defined as the drop in total pressure across a stage divided by the inlet dynamic head (see 3.1). Due to practical difficulties in getting the right inlet conditions for each traverse, a slightly different approach has been used here, giving repeatable and reliable results. This implies the assumption that the inlet total pressure is equal to the exit total pressure in the free-stream, well outside the wake.

To compute the loss, the mixed averaged total pressure is computed from the pitchwise total pressure profile with the wake, giving $p^{mixed}_{tot,\,wake}$. The mixed averaging process is momentum conservative and gives the average total pressure after the mixing process of the wake with the free stream.

The mixed averaged free-stream total pressure $p^{mixed}_{tot,\,free\text{-}stream}$ is also needed. To compute it, the wake is manually eliminated from the measured profile.

The experimental loss coefficient Y_p^{EXP} is finally computed as given in following equation and expressed in percentage.

$$Y_p^{EXP} = \frac{p^{mixed}_{tot,\,free\text{-}stream} - p^{mixed}_{tot,\,wake}}{p_{tot,\,in} - p_{in}} \qquad \textit{Eq. 5.4-4}$$

To improve the accuracy, many traverses have been run and the mean of each result has been taken. For blade B for example, the biggest difference between the value from a single experiment and the mean was around 0,5%. Since the mean value is 3,3%, this corresponds to 15% of the mean.

5.5 HOT WIRE ANEMOMETRY

5.5.1 OVERVIEW

Hot wire anemometry is a relatively simple and powerful tool to get unsteady velocity data at high sampling frequency. This allows the investigation of phenomena like the unsteadiness of the boundary layer caused by the interaction with the wakes coming from the upstream blade row.

A hotwire probe has been traversed in the boundary layer near the trailing edge of the three tested blades, at mid-height. The goal was to measure the unsteady momentum thickness to quantify the profile loss and to investigate the unsteadiness in the boundary layer and the effect of wakes.

5.5.2 OPERATING PRINCIPLE

A hot wire probe consists in a short, very thin, cylindrical resistance wire mounted on a probe. The length is usually one or two millimetres; the diameter is a few microns. Due to its small size, a very high spatial resolution is achievable, allowing for example traversing inside boundary layers. Furthermore, the thermal inertia of the wire is very small. This gives a very high frequency response, allowing the investigation of unsteady phenomena and turbulence with a sampling frequency up to 60 kHz (see 5.5.8).

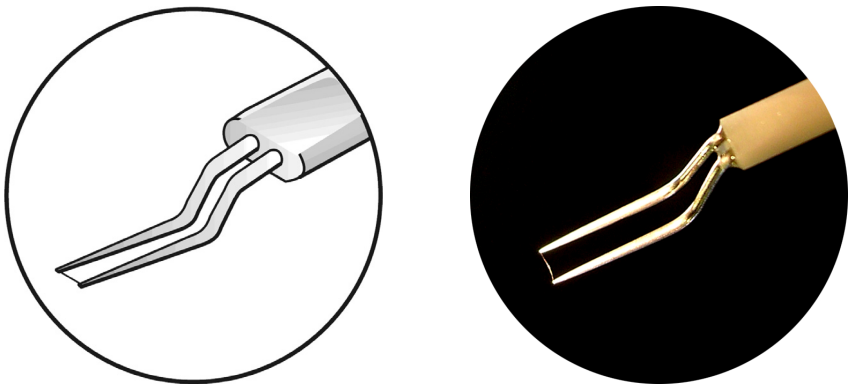

Figure 5.5-1: Boundary layer hot-wire, cartoon and real probe

The technique depends on the heat loss from the electrically heated probe to the surrounding fluid. The convective heat transfer is a function of the fluid velocity and the heat loss is equal to the electrical power delivered to the resistance. The ohmic resistance is kept constant by the electronic arrangement (see paragraph 5.5.3); therefore the electrical power is proportional to the square of the voltage across the wire. Thus, a relation between fluid velocity and probe voltage can be derived. This is known as Kings Law.

$$E^2 = E_0{}^2 + A \cdot |u|^n \qquad \textit{Eq. 5.5-1}$$

E is the voltage across the wire, u is the fluid velocity. A, E_0 and the exponent n are calibration constants, where E_0 is the voltage with no flow.

Self explanatorily, the heat transfer is only a function of the magnitude of u; no information about the direction of the velocity can be extrapolated from hot wire measurements.

5.5.3 ELECTRONIC ARRANGEMENT

In CTA (constant temperature anemometry) the temperature and therefore the ohmic resistance of the wire are kept constant. For this purpose, the relatively simple electronic circuit (called hot wire bridge) shown below is used.

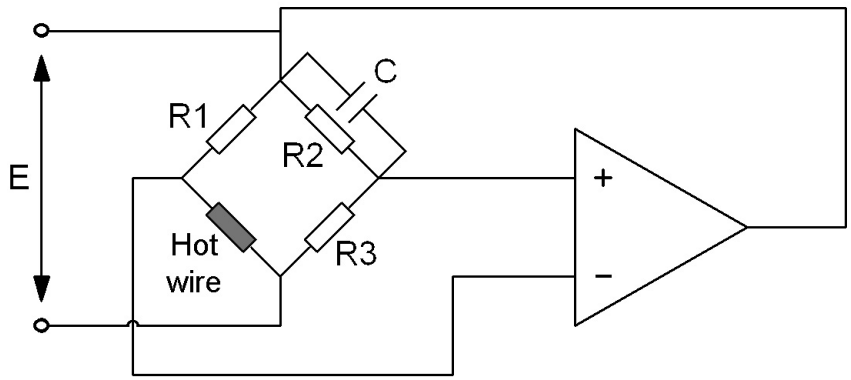

Figure 5.5-2: Schematic of electrical circuit for CTA

Assuming the bridge balanced at a certain condition, a change in the fluid velocity would change the temperature of the wire and therefore its resistance, making the bridge unbalanced. An increase in the air velocity would for example cause a decrease in the temperature of the wire and therefore in its resistance[1]. The bridge would be unbalanced and the amplifier would get a positive error voltage as input, rising the bridge voltage and with it the current through the wire. The temperature and the resistance of the wire would rise to the initial value and bridge balance would be restored.

5.5.4 PROBE CALIBRATION

A series of velocity measurements is taken in a calibration facility, where the dynamic head is also logged. The square of the logged voltage is plotted against the flow velocity at the n^{th} power and the exponent n is varied iteratively until the data points fit a straight line, according to Kings Law. The coefficients E_0 and A are finally extracted from the equation of the linear fit.

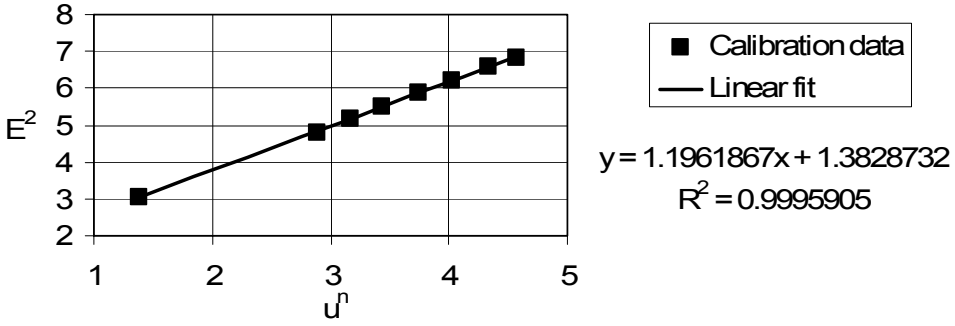

Figure 5.5-3: Typical calibration curve, n=0,402

[1] In metallic conductors, the resistivity grows linearly with increasing temperature according to $\rho = \rho_0[1 + k(T - T_0)]$, where k is a positive constant. A temperature drop gives then a lower resistance.

5.5.5 BEARMAN CORRECTION

The hot-wire technique is very sensitive to the ambient temperature. Because of the long run times for a hot-wire traverse and the different ambient conditions between calibration and measurements, the Bearman correction for the temperature must be used. The measured voltage E_{meas} is adjusted taking into account the difference between the measured temperature T_{meas} and a chosen reference temperature T_{ref} (20°C). The overheat ratio OHR is 1,8.

$$E = E_{meas} \cdot \left[1 - \frac{\frac{T_{ref} - T_{meas}}{T_{ref}}}{2 \cdot (OHR - 1)} \right] \qquad \textit{Eq. 5.5-2}$$

5.5.6 COX CORRECTION

The heat transfer from the hot wire to the surrounding environment is affected by the presence of walls. This is because the radiation heat transfer cannot be neglected in proximity of walls. In the case of a boundary layer traverse, this effect must be taken into account. The Cox correction is therefore applied. This is based on the voltage logged during a traverse performed without flow. The Kings Law is modified as reported in next equation.

$$E(y)^2 = E_0^{\,2} \cdot \left[\frac{E_0^{\,2}(y)}{E_0^{\,2}(\infty)} \right]_{no\ flow} + B \cdot u(y)^n \qquad \textit{Eq. 5.5-3}$$

5.5.7 POSITIONING

The wire should be positioned as near as possible to the blade surface. For this purpose, the blade is coated with a stripe of a conductive aluminium tape and the wire is carefully moved toward the blade surface until an electrical connection is established, and then a few motor steps back. A dial gauge is used to set the zero-position and ensure the repeatability of the positioning between different runs. Care has also been taken to ensure that the wire was perfectly parallel to the surface. The aluminium tape covers also the pressure tappings and ensures a uniform surface roughness.

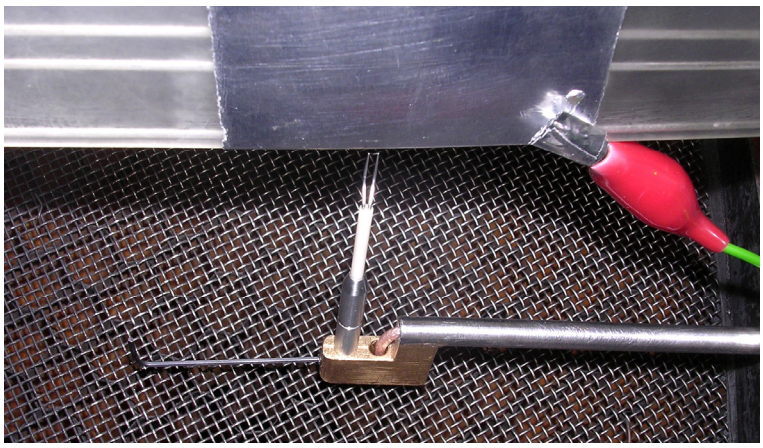

Figure 5.5-4: Positioning the hot wire

The wire should be positioned as near as possible to the trailing edge. Practically, the probe has been positioned on the suction surface, very near to the tangent point with the trailing edge circle.

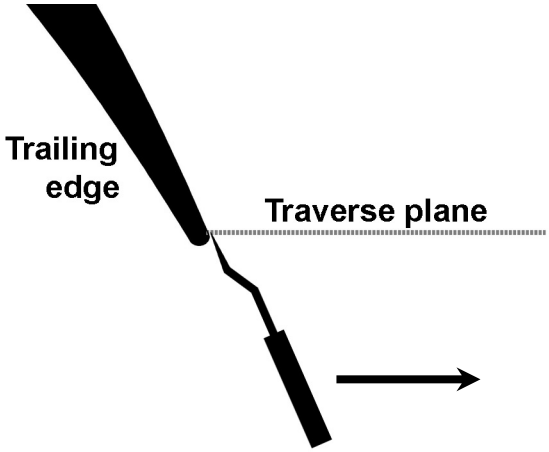

Figure 5.5-5: Hot wire traverse

5.5.8 DATA ACQUISITION

A LabVIEW program manages the movement of the traverse gear and the acquisition of the signal from the hot wire bridge and monitors all important variables like ambient conditions, rotor rpm and flow coefficient.

Two voltage signals are logged: a raw, unfiltered signal (DC) and a filtered one (AC). To get the AC signal, a lowpass filter with cut-off frequency of 30 kHz and a highpass at 0.1 kHz is applied to the raw signal. Both signals are acquired in ensembles, each consisting on 1024 single samples. 64 unfiltered ensembles and 128 filtered ensembles are logged. The acquisition of the signals is triggered by a light gate on the rotor providing a one per revolution

pulse. With this method, all the ensembles are acquired in phase and each of them contains for example the trace left by the wake originating from the same rotor blades. Sampling at 60 kHz, with a blade passing frequency of 425 Hz (500 rpm and 51 rotor blades in the annulus), a single ensemble of 1024 samples corresponds roughly to seven periods.

A single traverse starts on the blade surface and covers roughly half a passage. The points, 80 in total, are denser near the blade to accurately resolve all phenomena occurring in the boundary layer. The traverse slot is vertical to allow the probe o be traversed circumferentially, but the suction surface near the trailing edge has an angle of roughly 20 degrees. Therefore there can be some phase shift between data taken at different traverse position.

5.5.9 POST PROCESSING

Matlab scripts are used to post process the data and plot the results.

In each traverse position the DC signal is time averaged and is added to the AC signal, then the ensemble average of the 128 resulting ensembles is computed. Basing of this ensemble averaged data; all the needed boundary layer integral parameters are computed according to their definition.

Furthermore, a triple decomposition according to next equation has been applied to the velocity field.

$$u = \overline{u} + u'_{deterministic} + u'_{random} \qquad \textit{Eq. 5.5-4}$$

The random part has been computed as the root mean square value of the difference between each ensemble and the ensemble average.

Finally, the turbulence level has been computed dividing the random component by the local ensemble averaged velocity.

6 EXPERIMENTAL RESULTS

6.1 C_P MEASUREMENTS

The measured c_p profile for the three blades is here plotted against the non dimensionalised surface length s. As a comparison, the profile computed by MISES is also shown. The spike at the leading edge (dashed rectangle, zoomed in the left plot) is finely resolved. Some difference in the peak suction point and generally in the suction surface profile is present. As explained in 6.2.1, this is probably due to some three dimensional flow features, which can not be taken into account by Mises. This difference is more or less consistent for the three blades.

On the baseline blade, the spike is relatively narrow and sharp, as predicted by the CFD. It is slightly higher and wider than the computed one. No separation bubble could be observed, it is therefore difficult to assess where transition occurs. In any case, the results do not show it to happen at the leading edge, a certain fraction of the surface can be assumed to be laminar.

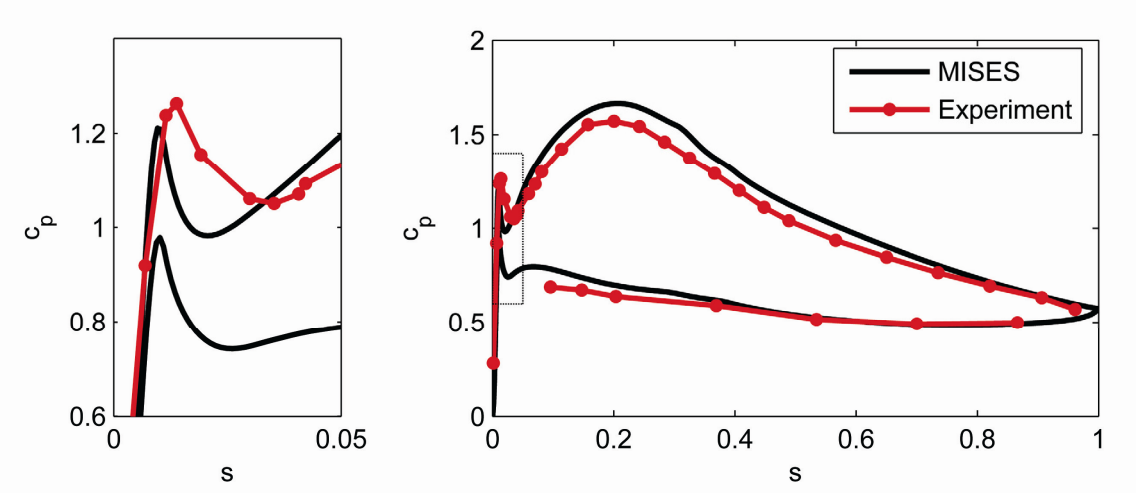

Figure 6.1-1: Measured c_p profile of blade A and Mises prediction

A sharp and much higher spike is present on blade B. Thanks to the high resolution given by the particular pepper pot design of the leading edge (see Figure 3.4-3), the separation bubble on both surfaces could be captured in the experiment. It is shown by the small region of more or less constant static pressure on the surface (red circles in the blow-up plot).

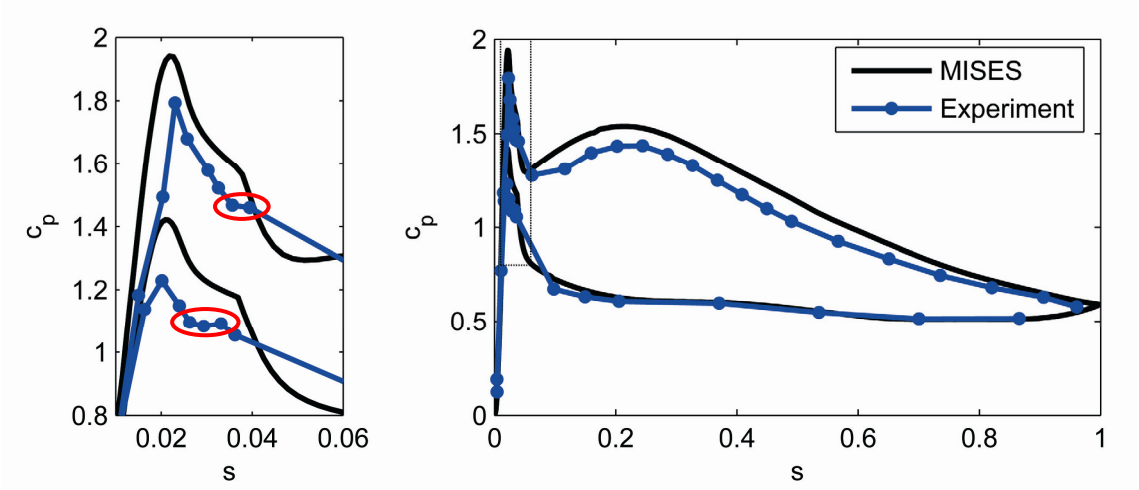

Figure 6.1-2: Measured c_p profile of blade B and Mises prediction

As explained in paragraph 2.1.1, the reattached boundary layer is turbulent. This leads to the conclusion that the boundary layer on the whole blade is turbulent, that is in agreement with Mises prediction.

The different geometry of blade C leads to a lower and less sharp spike. Similarly to blade A, no leading edge separation bubble on the suction side could be observed. Again, the boundary layer of part of the suction surface is likely to be laminar.

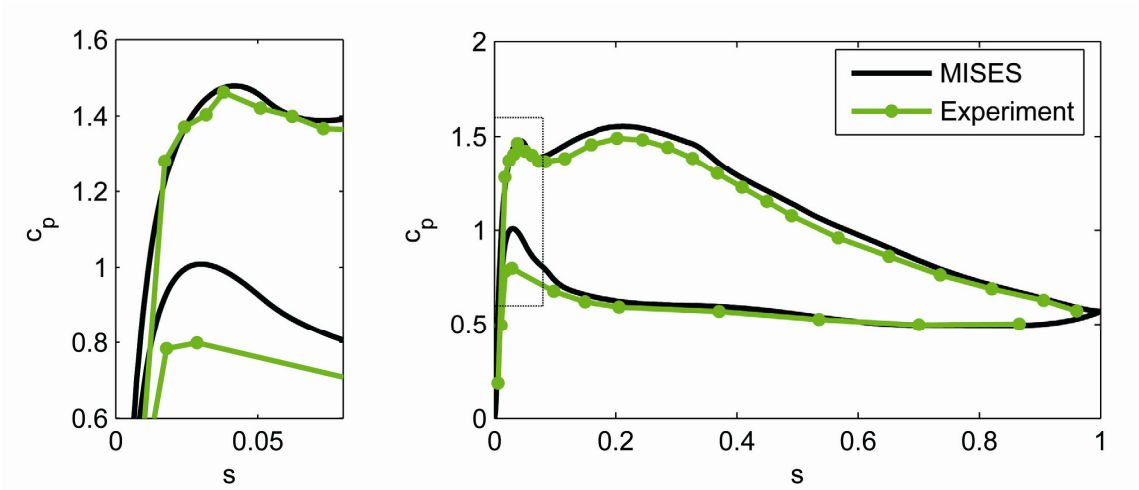

Figure 6.1-3: Measured c_p profile of blade C and Mises prediction

The measured pressure surface spike is considerably lower than the computed one. Mises predicted a separation on the pressure surface; this does not appear in the experimental data.

6.2 FLOW VISUALIZATION

6.2.1 THREE DIMENSIONAL FEATURES

The flow inside an axial compressor is three dimensional but the measurements have been taken only at mid height, assuming a two dimensional behaviour. To investigate if this assumption was appropriate, some flow visualization was necessary, aiming to show any three dimensional feature of the flow around the test blades. A wide black tape has been used to protect the tappings and to improve the contrast and the visibility of the dye traces.

The result of the oil & dye technique on blade A is shown in following figure. Some endwall separation can be observed at the tip and especially at the hub. The flow looks nearly two dimensional at mid height; however, because of the blockage at the endwalls, the axial velocity density ratio may be different from the one used in the computation. This is probably one of the reasons for the differences between measurements and CFD.

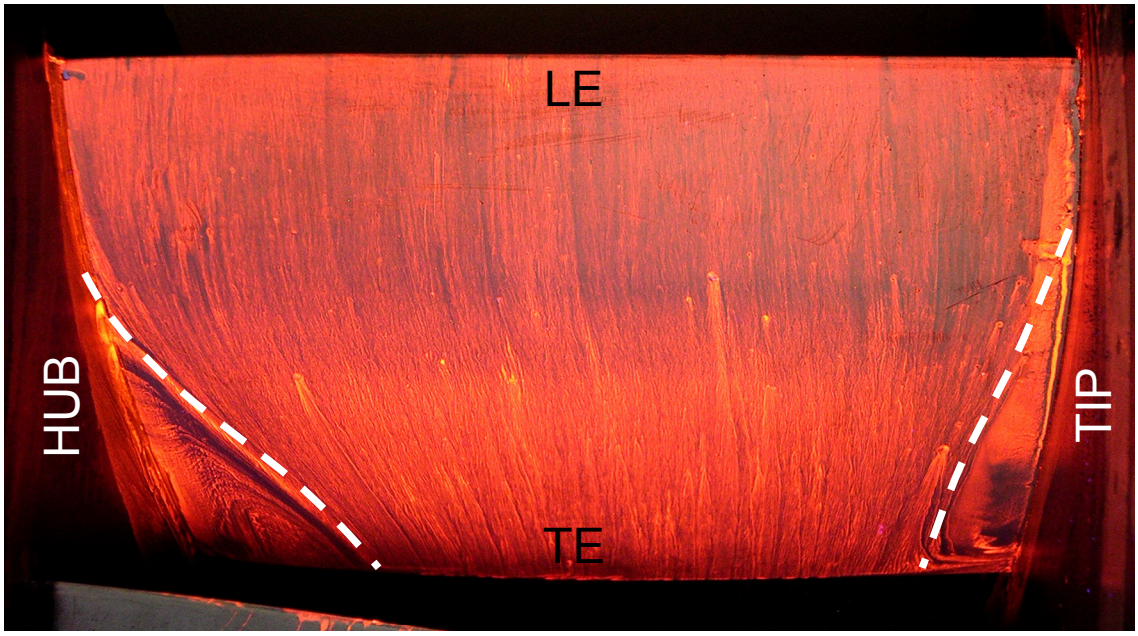

Figure 6.2-1: Flow visualization, blade A

A flow visualization of blade B is shown in next figure. In this case, the separation at the hub is much larger and the flow at mid height cannot be assumed to be two dimensional any more.

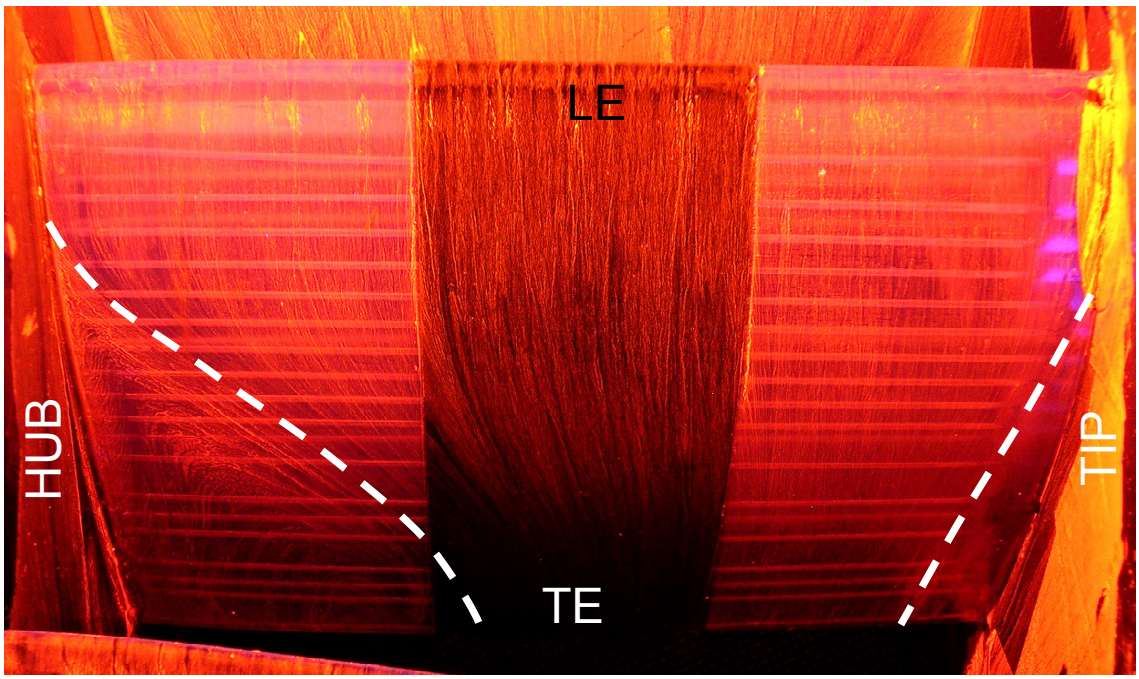

Figure 6.2-2: Flow visualization, blade B

It is believed that this difference is due to the different character of the suction side boundary layer of this blade. The leading edge trips the boundary layer making it turbulent and changing its properties. The boundary layer is probably more prone to separate; this allows the endwall separation to grow. This hypothesis is confirmed by next figure, where the time mean boundary layer profiles (from hotwire data) are given. B clearly shows a higher shape factor.

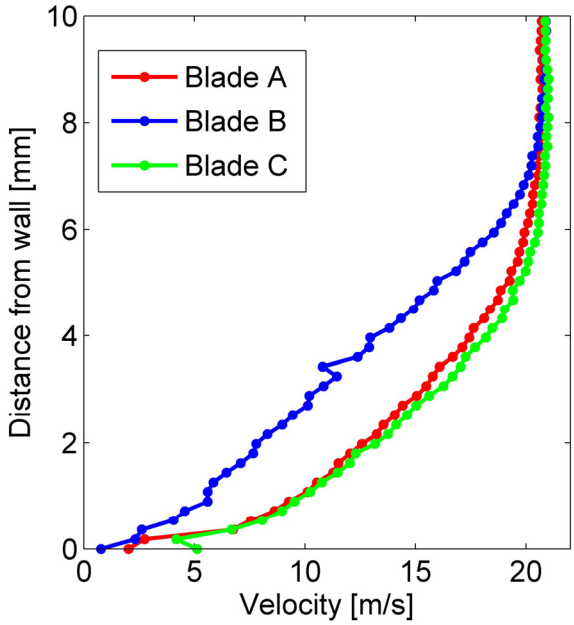

Figure 6.2-3: Time averaged boundary layers

A modification of the leading edge geometry has in this case a significant alteration of the characteristics of the flow in the entire passage, not only in the region of the leading edge. Anyway, this may be true for this specific geometry only; if such an effect can be generalized is questionable.

With such a configuration, any attempt to measure the c_p distribution showed a much worst agreement with the CFD computation. To correct this effect, the sealant at the hub has been removed, leaving an open gap (1,5 mm). As shown in next figure, this eliminated completely the separation at the hub, making the flow at mid height nearly two dimensional again. All the reported measurements have been taken with the gap unsealed.

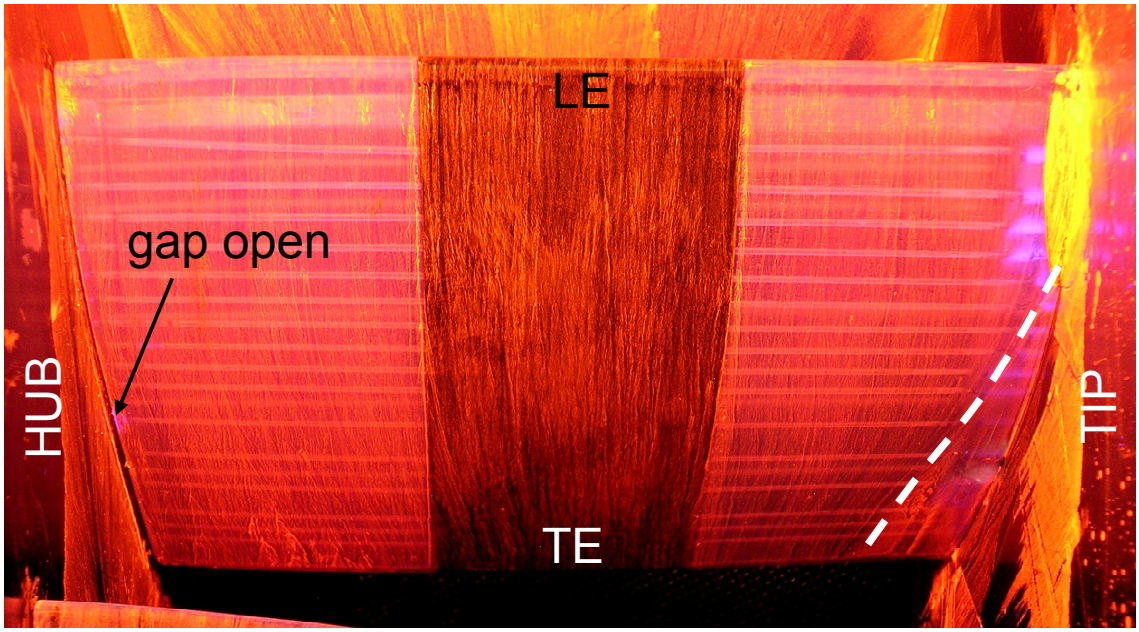

Figure 6.2-4: Flow visualization, blade B, hub gap unsealed

The same expedient has been used for blade C. Again, all the measurements have been taken with the hub gap open.

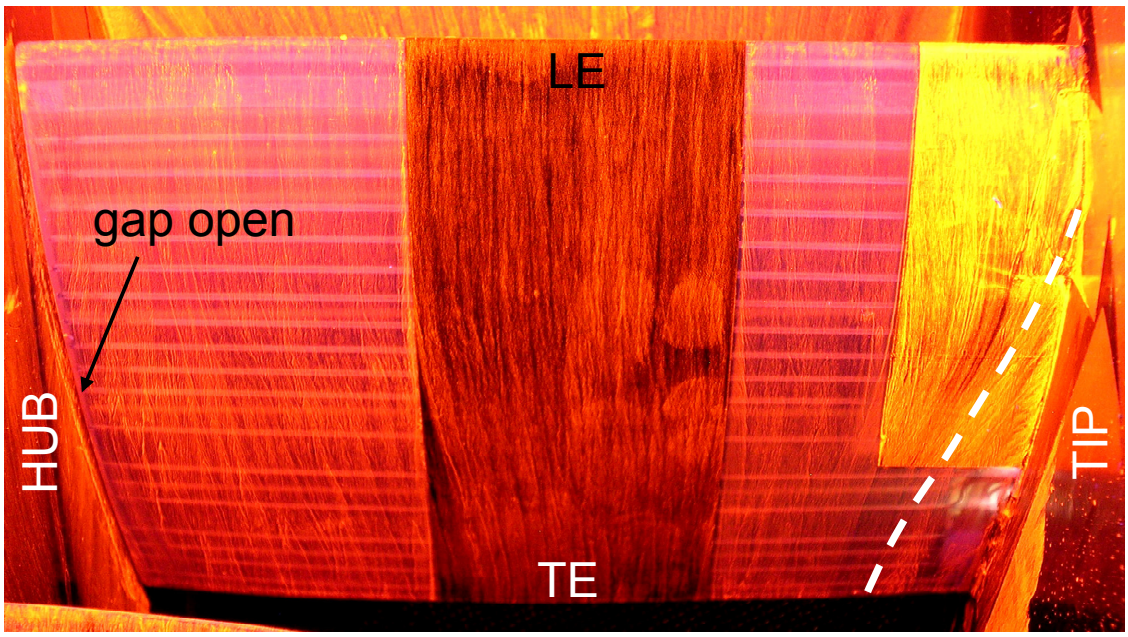

Figure 6.2-5: Flow visualization, blade C, hub gap unsealed

6.2.2 LEADING EDGE BUBBLE

Since the dye concentration is a function of the friction coefficient c_f, the flow visualization could also show the separation bubble at the leading edge of the blade B.

Within the bubble, c_f is very low and the dye accumulates giving a bright region. At the reattachment, the flow impinges and blows the dye away (high c_f), showing a darker zone. This pattern is very clear on the leading edge of the blade B, where a bright stripe followed by a dark one can be recognized. On the other hand, no separation can be observed on the blades A and C.

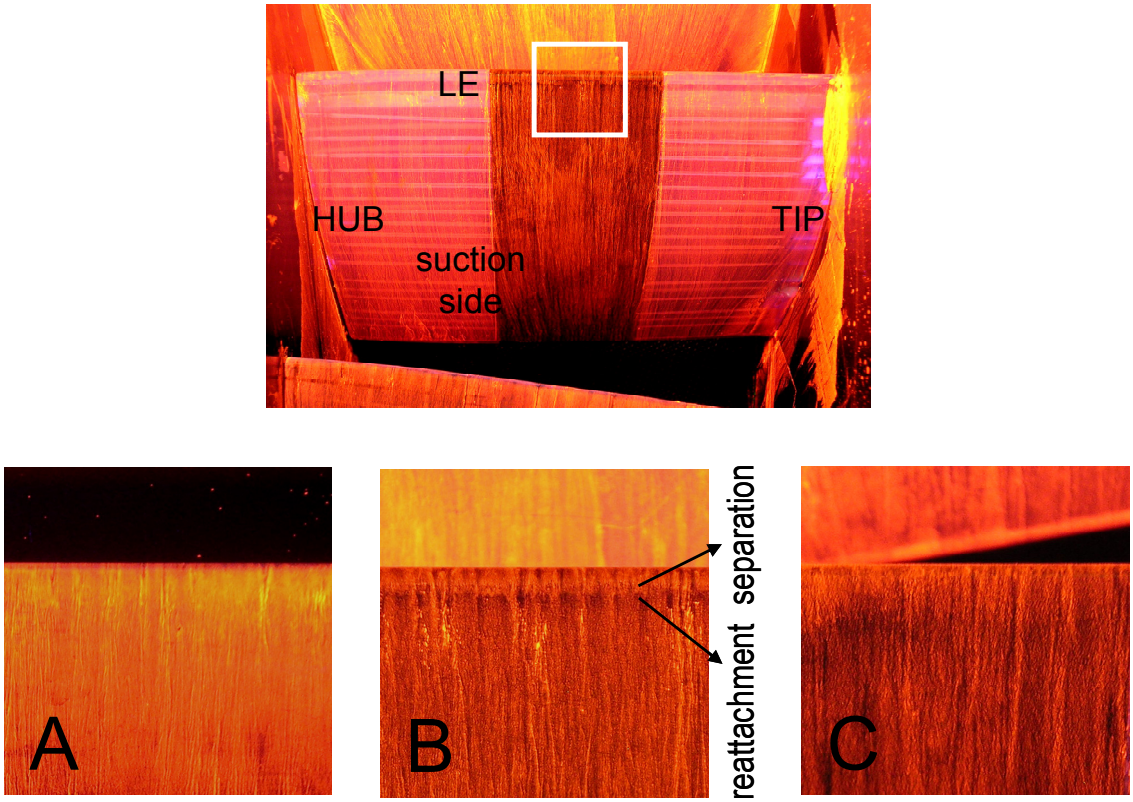

Figure 6.2-6: Visualization of leading edge separation bubble

6.3 WAKES AND LOSS

A three hole probe traverse downstream of the test blades allows the measurement of the pitchwise total pressure profiles, showing the wakes. The width and depth of the wake give a measure of the loss coefficient Y_p, as explained in 5.4.4. The wakes of the three test blades are plotted in next figure.

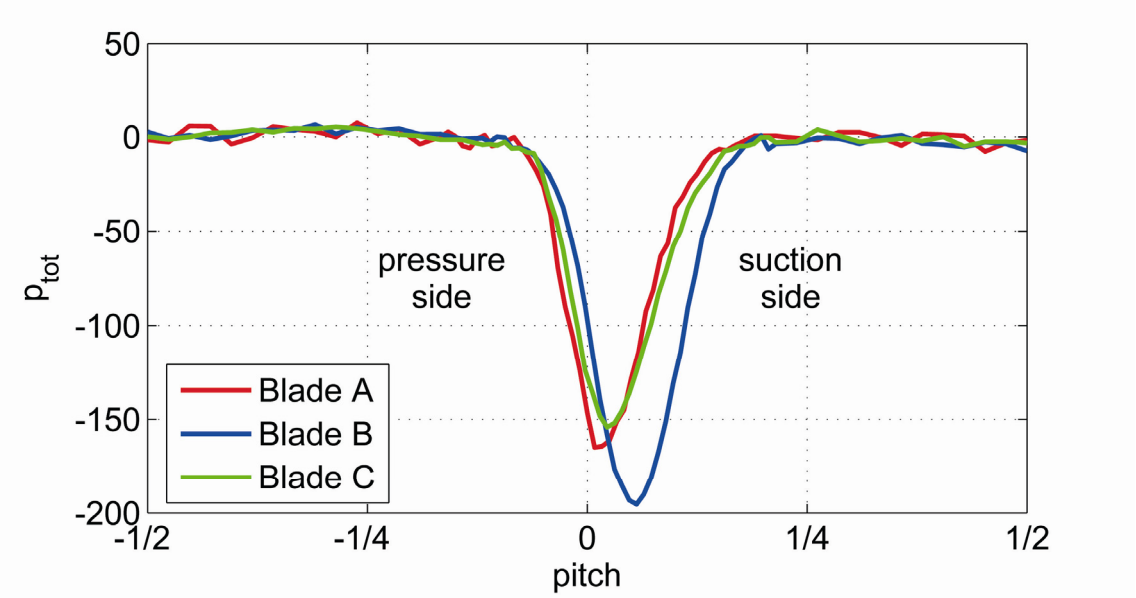

Figure 6.3-1: Wakes

The loss coefficients Y_p for the three blades are:

Blade A: Y_p=2,5%

Blade B: Y_p=3,3%

Blade C: Y_p=2,5%

Clearly, the highest loss value is associated with the widest and deepest wake: B. A and C have similar wake profiles and therefore similar loss.

The higher loss of blade B is due to the presence of the separation bubble. The reattached boundary layer is turbulent on the whole blade, leading to higher loss values. Moreover, across the bubble the momentum thickness grows significantly. This influences θ_{TE} and therefore the loss.

All experimental values are higher than the computed values. The difference between CFD and experiment is around 0,12% for blades A and C and roughly 0,17% for B. A higher discrepancy for B is consistent with the results shown in paragraph 6.4.1.

The wake B is also slightly shifted, showing a small difference in turning. This has been confirmed by the measurement of the exit flow angle: a difference of 0,9° has been measured.

6.4 UNSTEADY ANEMOMETRY

6.4.1 TRAILING EDGE MOMENTUM THICKNESS

The time resolved momentum thickness at the trailing edge θ_{TE} measured on the suction side with the hot wire is plotted in next figure for the three test cases. The lines represent Mises prediction.

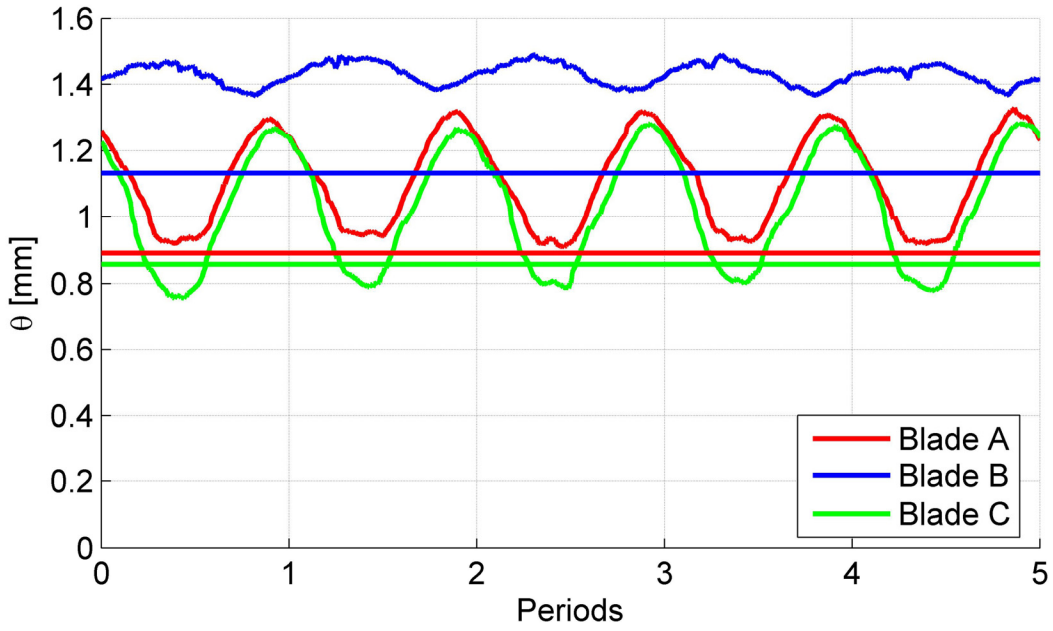

Figure 6.4-1: Suction side trailing edge momentum thickness

Consistently with the time averaged loss measurements reported in the previous paragraph, the highest θ_{TE} has been measured on blade B. Its value is also considerably higher than the value predicted by Mises. An explanation for that may be the low accuracy of Mises in predicting the right size of the separation bubble at the leading edge and therefore the value θ_0 just after the reattachment. As explained in paragraph 2.2, θ_0 has a key role in determining θ_{TE} and Y_p.

As expected, blades A and C have similar θ_{TE} values, slightly lower for C. If we assume that the value computed by Mises is the right value for steady flow, the previous figure shows that on blade A the effect of the unsteadiness induced by the wake is always negative, it raises the momentum thickness. θ_{TE} is always greater than or eventually equal to the steady value. This tends to exclude any becalmed region, which would show a value of θ_{TE} locally lower than the steady value.

This might be the case for blade C. Assuming again that Mises is correct, we can observe that θ drops periodically below the steady value. The presence of a becalmed region could be an explanation for it.

The mean trailing edge momentum thickness is apparently lower on blade C than on blade B. However, the loss measurements reported in the previous paragraph show practically the same loss. This is because the contribution of the pressure side is not considered here. This might be bigger for C (a separation bubble is likely to be present on the pressure surface, see chapter 4).

6.4.2 BOUNDARY LAYER UNSTEADINESS

The upstream rotor blades produce their own wakes, which hit the leading edge of the test blades and interact with their boundary layer. This interaction leads to unsteady phenomena in the boundary layer, which must be investigated to gain some understanding on the effect that the wakes have on the loss. In this case, the hotwire data have been used to give an interpretation of the transient behaviour of the trailing edge momentum thickness.

In Figure 6.4-2, the ensemble averaged velocity field is plotted together with the momentum thickness for the three blades. The flow field is represented in a space-time diagram, with the axes being respectively the distance from the wall surface and the blade passing periods.

Regions of locally lower velocity can be observed in the free stream. These appear like yellow stripes (marked with W) and are believed to be the wakes, as confirmed later. Near the wall, a lower velocity region shows clearly the boundary layer. Significant velocity fluctuation in the boundary layer is present on blades A and C, their flow field appear to be very similar. On the other hand, on blade B, the wakes are still recognisable but the boundary layer looks very different, almost steady.

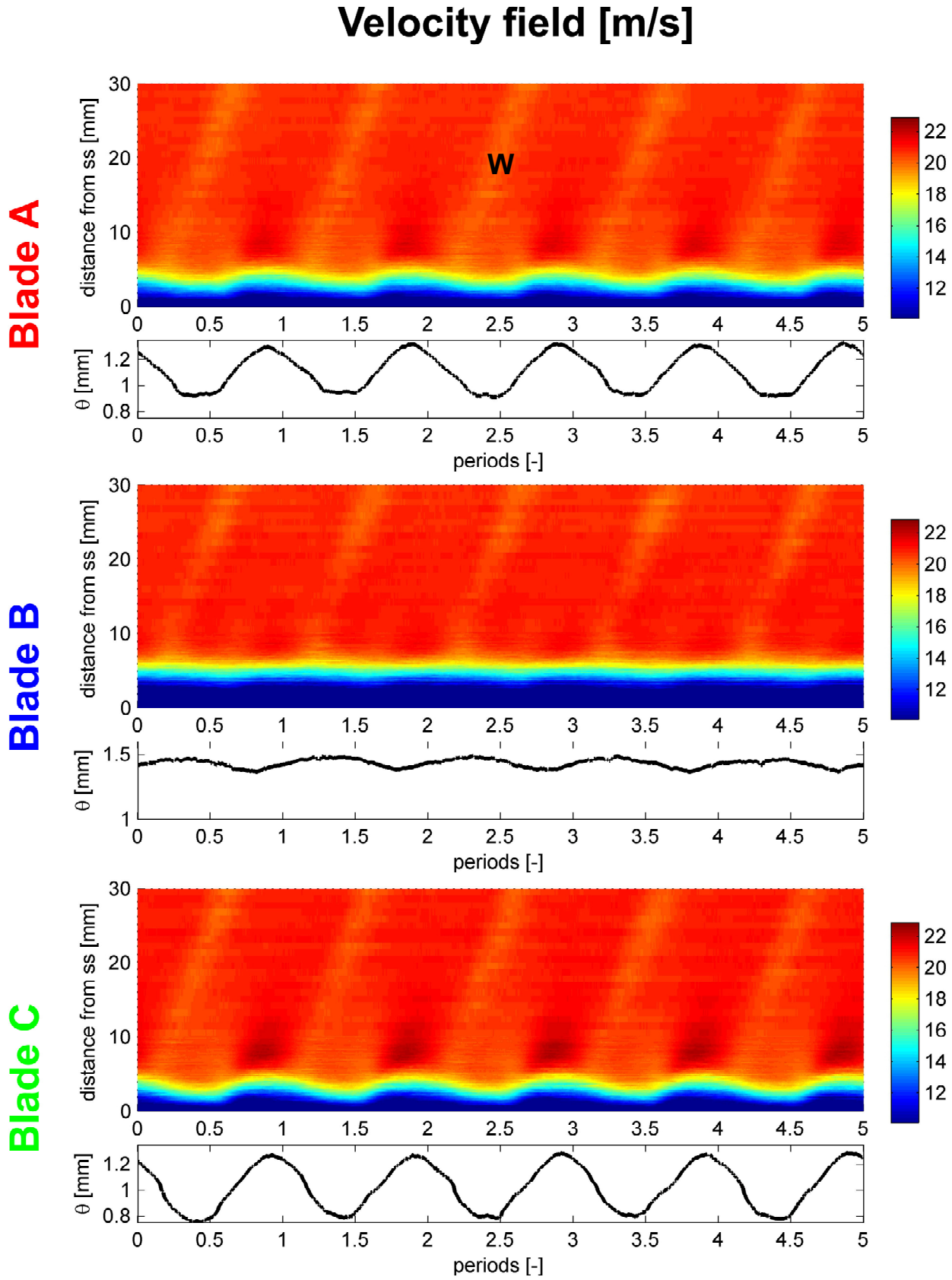

Figure 6.4-2: Velocity field, ensemble average

To better resolve the velocity fluctuations, the perturbation of the velocity field is presented in Figure 6.4-3. This is found subtracting the time mean from the velocity field.

A “four-leaf” pattern (marked with F) can be observed near the surface, showing symmetrically two high velocity and two low velocity regions. The perturbations are higher near the wall. The pattern is very clear in blades A and C (with a higher intensity in C). It is also present in B, but its intensity is much lower.

The low velocity region near the wall is in phase with the peak in momentum thickness. It is marked with P.

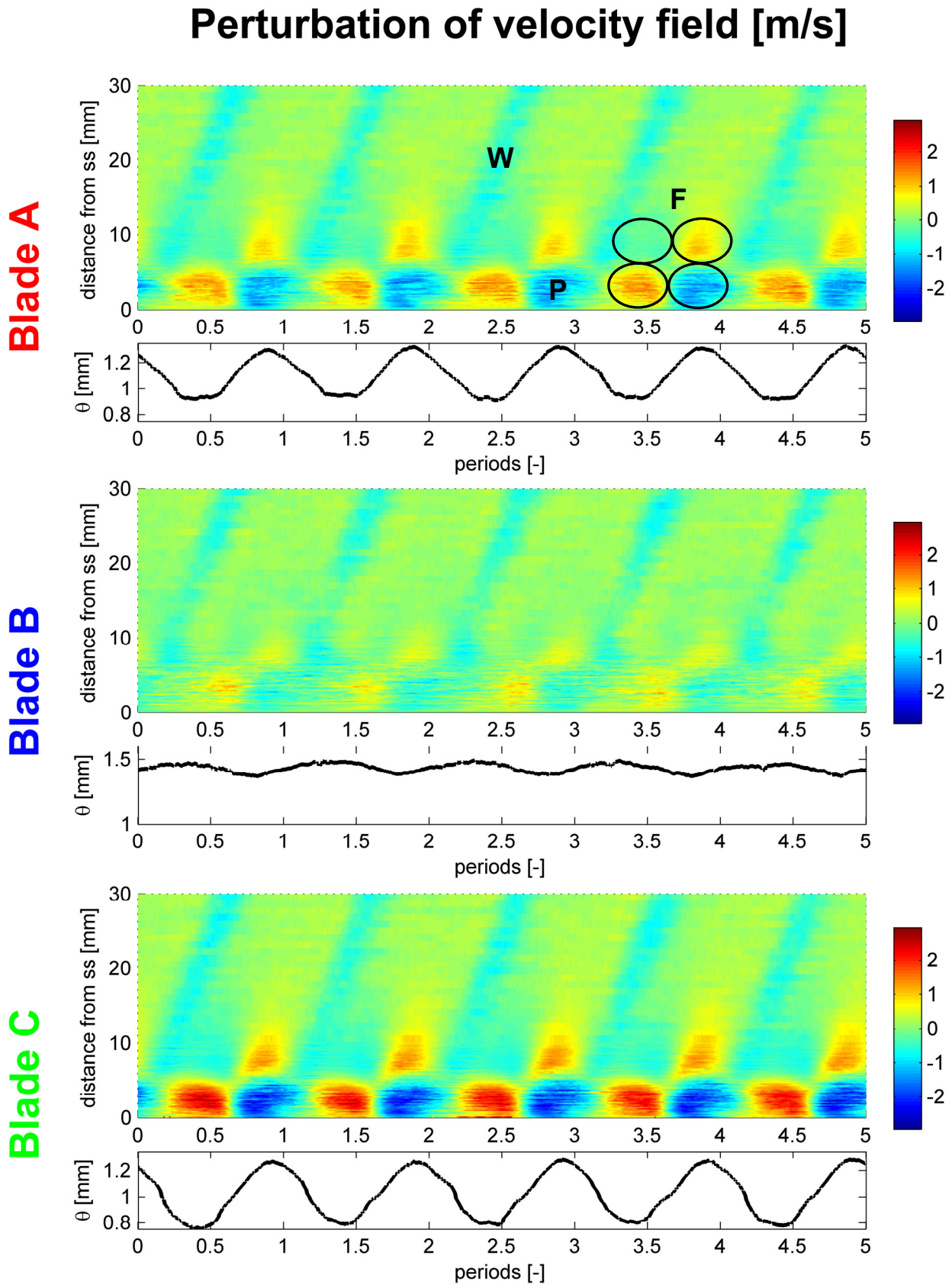

Figure 6.4-3: Perturbation of velocity field

As further investigation, the turbulence of the flow inside the boundary layer has been computed. This is presented in Figure 6.4-4 as the random part of the velocity field and in figures Figure 6.4-5 as the turbulence level (random part divided by the local velocity).

The wakes are again well visible. These are shown by a higher turbulence. These light blue stripes are in phase with the yellow stripes of previous plots, showing that the low velocity stripes observed were really the wakes.

A turbulence peak in the boundary layer is clearly identified in A and C. This structure appeared in the previous graphs as the low velocity region; it is in phase with the peak in the momentum thickness and is marked again with P. It is therefore clear that some loss generation mechanism must be associated with it, leading to the peak in the momentum thickness. The percentage turbulence level shows that the structures are not detached from the wall as they could appear in Figure 6.4-4.

As shown in 2.3.3, the vortical structure presented in [9] and [10] are also in phase with the peaks in the momentum thickness. Therefore, it can be assumed that those vortical structures and the turbulent peaks shown here are actually different manifestations of the same entity: a wake induced structure convecting inside the boundary layer.

Interestingly, the high values in θ_{TE} in A and C are not in phase in the wake: the wake has apparently no direct effect on it. However, the incoming wakes are believed to be the cause for the structures to appear. As presented in [10] and reassumed in chapter 2.3.3, the turbulent structures and the wakes are in phase at the leading edge. The structure P is induced by the wake as it hits the leading edge of the blade and convects behind it along the surface. The phase delay of the structure is given by its lower convective velocity. A slight difference in this phase delay is observed between the blade A and C, this might be the effect of a different convective velocity of the structure induced by the difference in the profile.

In blade B, the peak P cannot be identified. The different leading edge shape gives simply different flow physics of the boundary layer. However, due to the results shown in Figure 6.4-3 (flow field perturbation) and described in page 64, it is believed that a similar structure should be observable also in this case. Anyway, no appreciable peak in the trailing edge momentum thickness is present in phase with it.

Actually, in blade B, the small peaks in the trailing edge momentum thickness appear to be in phase with the wakes. This seems in contradiction with the comments above. However, the figures show different boundary layer characters in this case; a different phase relation between θ_{TE} cannot therefore be excluded. Moreover, the low peak present in the trailing edge momentum thickness might also be given by some inaccuracy in the post processing (the integration domain for the computation of θ might be slightly too large, including part of the wake). The same should actually happen in A and C, but since θ_{TE} oscillates widely, such a small variation is hard to recognize.

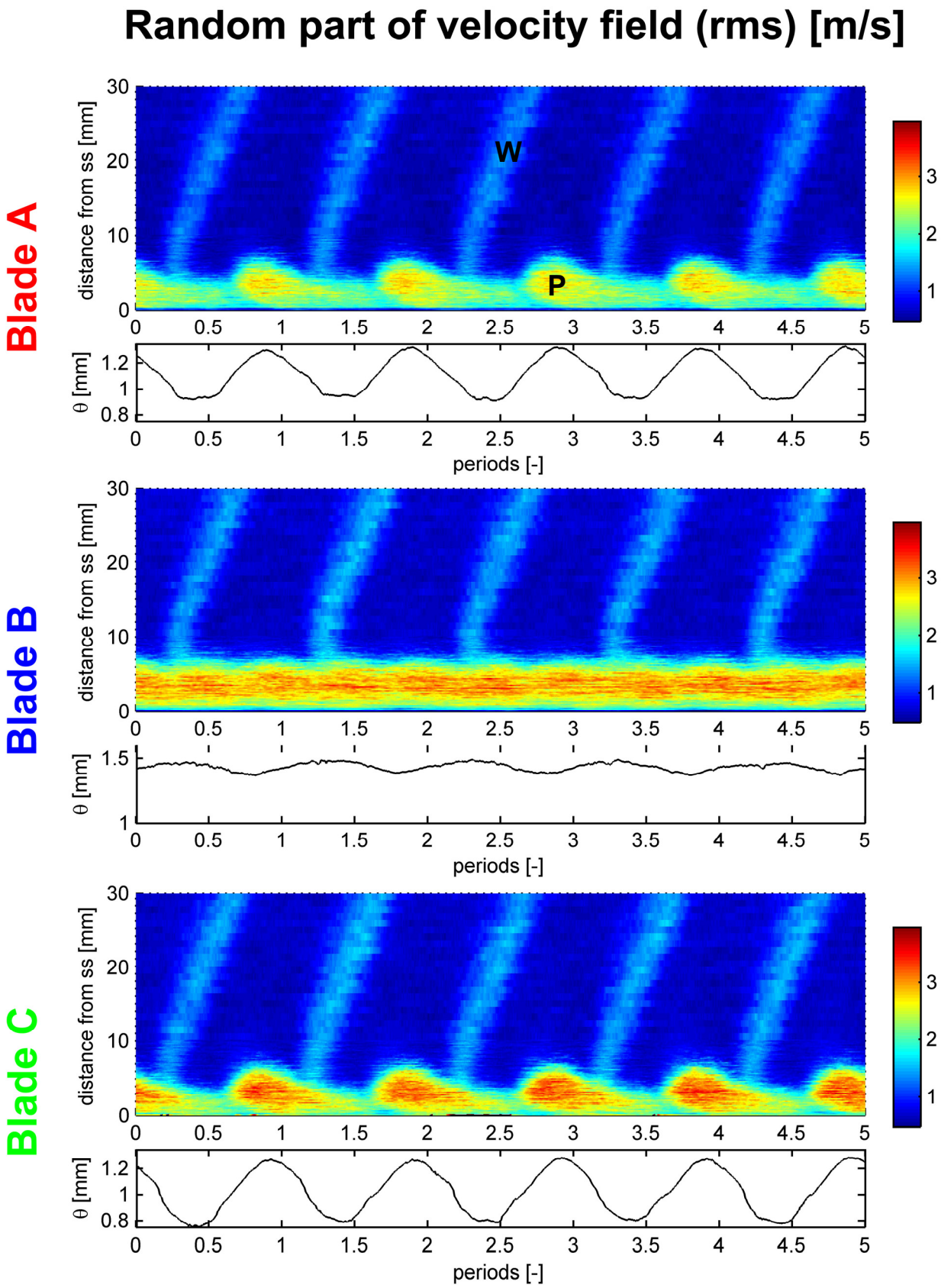

Figure 6.4-4: Random part of velocity field

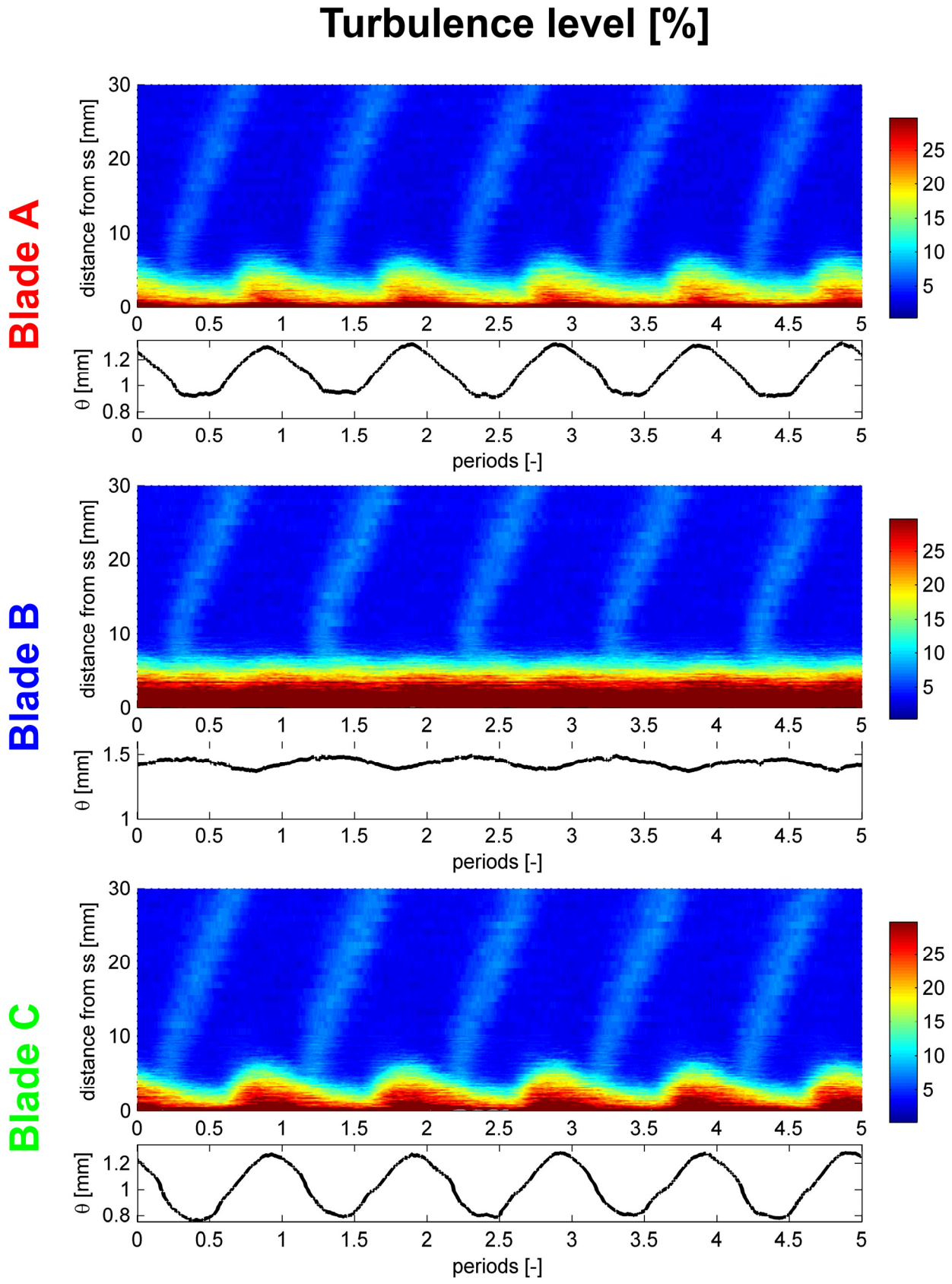

Figure 6.4-5: Turbulence level and momentum thickness

7 SUMMARY AND CONCLUSIONS

Starting from the baseline stator blade of the Deverson rig (circular leading edge and 32° wedge angle), two new geometries have been designed. The new blades have a 15° wedge angle and a circular and an elliptic (3:1) leading edge, respectively. Their leading edge geometry is therefore more representative of a real engine blade.

The three test cases are: A: 32° wedge angle, circular leading edge;
B: 15° wedge angle, circular leading edge;
C: 15° wedge angle, elliptic (3:1) leading edge.

A CFD analysis using the two dimensional, steady code Mises has been performed on the three test cases, at mid-height.

Three fully instrumented prototype blades have been built and tested in the Deverson rig, a low speed, single stage, axial flow compressor. All the investigations have been performed at mid-height. The c_p distribution has been measured using the pressure tappings, with a very fine resolution at the leading edge, to capture the suction spike and eventually the separation bubble. Three hole probe traverses have been performed, allowing to measure the wake of the test blades and to get a time averaged loss coefficient Y_p. Finally, a hot wire has been traversed in the boundary layer at the trailing edge, providing an unsteady measurement of the trailing edge momentum thickness. The hot wire data were also used to investigate the unsteady phenomena in the boundary layer due to the effect of the wakes of the upstream blade row.

With a 15° wedge angle, a comparison between the elliptic and the circular leading edge has shown significant advantages for the elliptic shape. Y_p is 3,3% for blade B and only 2,5% for C, that is about 25% less. The trailing edge momentum thickness θ_{TE} drops from 1,43 mm up to 1,02 mm (mean) for C. The behaviour and performances of the high wedge angle blade A (Y_p is 2,5% and the mean θ_{TE} is 1,10 mm) are very similar to those of blade C.

The explanation for this difference is in the separation bubble occurring at the wedge point of the circular leading edge. This was clearly shown in the flow visualization and in the c_p measurements on blade B as well as in Mises results. Across the bubble, the momentum thickness grows significantly, influ-

encing θ_{TE} and therefore the loss. Moreover, the reattached boundary layer is turbulent on the whole blade, leading to higher loss values.

On blades A and C no separation is present. The high wedge angle and the elliptic leading edge have the effect to suppress it. The spikes are much lower and the boundary layers are laminar for a significant percentage of the chord (about 20%).

However, the circular leading edge blade with the separation bubble appears to be less influenced by the unsteadiness induced by the wake. The boundary layer of B looks almost steady and small θ_{TE} fluctuations (8%) have been recorded. On the other hand, a structure convecting behind the wake has been measured as a turbulence peak in the boundary layer of A and C. This caused wide fluctuations of θ_{TE} (51% and 38%, respectively).

To conclude, this work shows very clearly that the separation bubble must be avoided to keep the loss low. To do this, the leading edge must be properly designed. For low wedge angle blades such real compressor blades, an elliptic leading edge is significantly better than a circular one. A 25% drop in Y_p can be achieved.

8 SUGGESTIONS FOR FUTURE INVESTIGATIONS

8.1 FURTHER INVESTIGATION ON THE PRESENT TEST BLADES

The results of this work are consistent with those presented in [9] and [10]. Those results are based on measurements done on the baseline blade A. It might be therefore interesting to repeat some of the PIV or hot film investigations on the new geometry.

Similar results are to be expected on blade C, some difference in the intensity and convective velocity of the boundary layer structures are likely.

Blade B showed the worst performances. From this point of view, further investigations seem to be useless. But, on the other hand, blade B shows a completely different physics: a different behaviour of the boundary layer and probably different mechanisms of wake-leading edge interaction. For this reason, additional studies could bring interesting new results and let us gain some more understanding of the physics of the problem.

8.2 NEW GEOMETRIES

The goal of this project was not to design the best possible leading edge; no optimisation has been performed and the chosen leading edge geometries were rather simple. This has shown a good potential for improvement. Many other geometries could be tested: ellipses with different axes ratio, parabolic or hyperbolic leading edges, even asymmetric leading edges. This may lead to the final goal of designing optimised geometries with better performances.

For example: since the wake causes generally higher incidence, the leading edge might be slightly drooped. This may lead to an improved behaviour when the wake hits the leading edge.

However, manufacturing issues must be kept in mind. Compressor blades are usually relatively small and the manufacturing of rather complicated geometries might end up being almost impossible. The effect of erosion during the service must be also taken into account.

8.3 THREE DIMENSIONAL PHENOMENA

The flow visualization results show clearly that the modification of the leading edge could lead to some initially unexpected phenomena like for example endwall separations. This represented rather a problem for this work, since the task was a two dimensional analysis at mid height, and has been solved unsealing the hub gap.

It has been observed that the tripped boundary layer of blade B was more prone to separate (higher shape factor). The result was a significantly bigger corner stall. If the observed phenomena can be generalized or if it is specific for the tested geometry is still questionable; however, a deeper investigation of the effect of the leading edge geometry on the three dimensional behaviour of the flow (and specifically on the endwall flows) might be worth doing.

9 REFERENCES

[1] ARENA A. V., MÜLLER T. J., *Laminar separation, transition, and turbulent reattachment near the leading edge of airfoils*, AIAA Journal, Vol. 18, No. 7, pp. 747-753, 1980.

[2] BOLGER J. J., *Three Dimensional Design of Compressor Blades*, PhD dissertation, University of Cambridge, 1999.

[3] CUMPSTY N. A., *Compressor Aerodynamics*, Longman, 1990

[4] DRELA M., YOUNGREN H., *A User's Guide to MISES 2.53*, MIT Computational Aerospace Sciences Laboratory, 1998

[5] PLACE J. M. M., *Three-Dimensional Flow in Core Compressors*, PhD dissertation, University of Cambridge, 1997.

[6] TAIN L., *Compressor leading edges in compressible and incompressible flows*, PhD dissertation, University of Cambridge, 1999.

[7] TAIN L., CUMPSTY N. A., *Compressor blade leading edge in subsonic compressible flow*, Proc Instn Mech Engnrs Vol 214 Part C, 2000

[8] WALREAVENS R. E., CUMPSTY N. A., *Leading edge separation bubbles on turbomachine blades*, Trans. ASME J. Turbomachinery, Vol. 117, pp. 115-125, 1995.

[9] WHEELER A. P., MILLER R. J., HODSON H. P., *The effect of wakes induced structures on compressor boundary layers*, ASME Turbo Expo 2006, paper no. GT2006-98092.

[10] WHEELER A. P., *Unsteady flows in compressors*, PhD dissertation, University of Cambridge, to be submitted in 2007.

APPENDIX – MISES

A.1 DEFINITION AND INPUT DATA

The Mises system is a collection of programs for cascade analysis and design. This includes programs for grid generations and initialization, flow analysis, plotting and interpretation of the results, and an interactive program to specify design conditions.

Only a brief description of the most important features of Mises is given here. More information is to be found in [4].

The coordinates of the airfoil stored in an input file are defined in the m'–θ streamsurface coordinate system. θ is the circumferential angle while m' is the arc length projected onto the meridional r–z plane (m), non dimensionalised with the local radius.

$$m' = \int \frac{dm}{r} = \int \frac{\sqrt{dr^2 + dz^2}}{r} \qquad \textit{Eq. A-1}$$

The two-dimensional, periodical grid domain is the blade passage enclosed between two blades and their stagnation streamlines. The grid boundaries are defined through two parameters m'_1 and m'_2, as shown in figure.

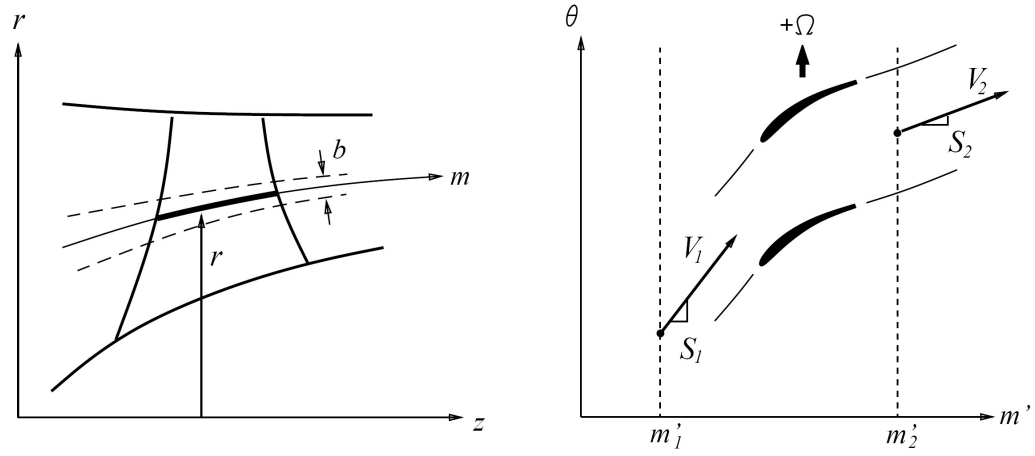

Figure A.1-1: Streamsurface

A streamtube definition file is also needed. It containes the streamsurface coordinates r(z) and the streamtube thickness b(z).

In this work, Matlab scripts have been used to import the blade and streamsurface data in r–θ–z coordinates and transform it into Mises m'–θ coordinates. For the streamtube thickness, the ration between inlet and exit area thickness has been computed from three hole probe measurements data taken from [2], then a linear streamwise variation has been assumed.

A flow condition file contains all the needed flow data such as Mach numbers, Reynolds number, turbulence level or inlet flow angle.

A.2 PROCEDURE

The grid initialization program reads the input data, builds the geometry and initialises the grid. The grid can be fully edited using the given options; the result can be stored in a grid parameter file.

When the computational domain and the grid are set, the computation is started. Two Newton iterations are performed in the inviscid mode, then the boundary layer is initialized and the viscous mode turns on and Newton iterations are performed until convergence. The program is very quick, less than 20 iterations (less than one minute) were usually enough to get convergence. A file containing the solution data is written. This will be the initial solution for any other further computation.

A third program is used to plot the results. Mach distribution, c_p profiles, boundary layer properties, and many other plots can be done. Some results on the test blades are shown in chapter 4.

The Mises system contains also programs for inverse calculation or to perform calculations varying specified parameters.